Probing Organization of Multiple Chains in Nanofluidic Device

Zezhou Liu

Master of Science in Physics

Department of Physics

McGill University

Montreal,Quebec

2018-11-01

A thesis submitted to McGill University in partial fulfillment of the requirements of the degree of Master of Science

©Zezhou Liu

DEDICATION

This document is dedicated to the graduate students of the McGill University.

ACKNOWLEDGEMENTS

Acknowledgments, if included, must be written in complete sentences. Do not use direct address. For example, instead of Thanks, Mom and Dad!, you should say I thank my parents.

ABSTRACT

A pneumatically-actuated nanofluidic platform that has the capability of dynamically controlling the confinement environment of macromolecules in solution is presented in this thesis. We use this system to quantify the interactions of multiple confined DNA chains, a key problem in polymer physics with important implications for nanofluidic device performance and DNA partitioning/organization in bacteria and the eukaryotes. To begin the thesis, the study of DNA dynamics in slit-like confinement is reviewed. The device fabrication method, the fast switching microscope setup and experiments we have done are followed after. Further, preliminary data of probing transition between different dynamical states as the confinement varied from quasi-0D (cavity confinement) to quasi 1-D (nanochannel confinement) is discussed at the end of the thesis.

ABRÉGÉ

TABLE OF CONTENTS

DEDICATION ii

ACKNOWLEDGEMENTS iii

ABSTRACT iv

ABRÉGÉ v

1 Introduction 1

1.1 Background and Motivation 1
1.2 DNA confinement 2
1.3 Fundamental parameters of DNA 4
1.3.1 Contour length 4
1.3.2 Radius of gyration 4
1.3.3 Persistence length 5
1.4 Microfluidics and Nanofluidics 7
1.5 Overview of this work 8

2 Review of slit-like confinement 10

2.1 Bulk regime 11
2.2 de Gennes regime 16
2.2.1 Chain conformation of de Gennes regime 16
2.2.2 Dynamics of de Gennes regime chain 18
2.2.3 Experiments in de Gennes regime 21
2.2.4 Simulations in de Gennes regime 23
2.3 Odijk regime 23
2.3.1 Theory of polymer in Odijk regime 24
2.3.2 Experiment in Odijk regime 26
2.3.3 Summary 27

3 Device fabrication 29

3.1 Device overview 30
3.2 Fabrication flow 30
3.3 Silicon wafer fabrication 32
3.4 Borofloat wafer fabrication 33
3.4.1 Alignment marks lift-off 34
3.4.2 Nano-cavity fabrication 37
3.4.3 Loading micro-channel fabrication 41
3.5 Anodic bonding 41
3.6 Backside alignment and KOH etching 43

4 Experiment setup 46

4.1 Chemical buffer 46
4.2 DNA sample 48
4.3 Pneumatic regulation system 50
4.4 Fluorescence microscopy 52
4.5 Fast switch LED system in fluorescence microscopy 57

5 Data analysis 62

5.1 Data format and the pre-process 63
5.1.1 DNA position analysis 65
5.2 DNA diffusion analysis for single chain trapping 69
5.2.1 Position auto-correlation calculation 72
5.2.2 Intensity cross-correlation function 74

6 Conclusion 77

6.1 Conclusion 77

7 Latest work in multiple chains system: chain swapping in a cavity 80

7.1 Fluorescence tracking 80
7.2 Position correlation 86
7.3 Position switching of two chains 87

REFERENCES 91

CHAPTER 1
Introduction

1.1 Background and Motivation

Behavior of multiple interacting DNA chains in a confined space is a fundamental topic in both polymer physics and biological systems, and has practical significance in technological applications. For instance, at prophase of cell division, long thin chromatin transforms into compact and transportable chromosomes. Compared with the length of DNA in a single human cell, which is approximately 2 meters[26], Human genome only consists of 23 pairs of chromosomes. Each single chromosome is roughly one or two micrometers long. The huge difference between the generic size of DNA and chromosome reveals that multiple DNA chains are confined within a limited space. Thus, DNA chains interact with each other physically by various mechanism, such as volume exclusive effect and so on.

How do DNA chains influence each other in cell? This question is so far mysterious and still interests many researchers. A recent work shows that condensed chromosomes structures are built by ring-shaped protein machines, which consume energy from ATP hydrolysis. Multiple DNA strands are able to be hold together within micrometer scales[52]. DNA strands interaction becomes physically interesting when the separation between strands is within micrometer scale, which is around the radius of gyration of DNA polymer. Polymer under confinement is studied by

several generations of physicists in past few decades. Thus, sophisticated physics study could provide some inspiring idea about the DNA interaction.

Beyond above, determining the sequence of the nucleotide bases is always the most concerning problem since it has profound benefits, genetic disease diagnostic for example. By combining the recent nanopore sequencing technology, Ji W Shim.et al[43] has performed a study with protein cavity and nanopore to investigate the folding and unfolding of the G-quadruplex, which is important to understand in gene regulation.

However, performance of protein cavity and protein pore rely on delicately controlled experimental condition. This requirement hinders the way to populate this technology. On the contrary, the solid-state diagnostic chips, which are made by the Microelectromechanical systems(MEMS) fabrication method, are more robust compared with the protein based chip. Inheriting the advantage of MEMS fabrication, solid-state chips can be produced in parallel style and has more accurate control on the feature dimensions. This project,developed from MEMS fabrication, provides a solid fabrication protocol for nanocavity-nanopore coupling system.

1.2 DNA confinement

Deoxyribonucleic acid, which is well known as DNA, behaves as the fundamental building blocks for various creatures. The simplest unit of DNA is nucleotide. There are four different kinds of nucleotide distinguished by different nitrogenous bases(cytosine[C], guanine[G], adenine[A] and thymine[T]). Those primal units are connected by the bonds between deoxyribose and phosphate base to form a single chain. Usually DNA is composed of two chains. These two chains coil and twist

around each other and have hydrogen bonds in between to form double helix structure. Base pairing rule only allows two kinds of nitrogenous bases pairs forming. Adenine has to bond with thymine and guanine has to bond with guanine. In living organisms, double strand DNA exists as the headquarter of cell. They store biological information, thus control the protein synthesis and replication of cell.

Usually DNA does not exist with a straight double helix chain form. They tend to twist with higher order complexity and form chromosome. Supercoiling, branch and G-quadruplex are three very interesting and attractive conformation so far for researchers. Physically, the conformation of DNA should minimize the free energy of the system. Thus, how to construct the free energy describing DNA conformation is still a debating question[17, 24, 21]. Polymer physics is a physics field investigating polymer conformation and dynamics. On the other hand, DNA can be treated as a semi-flexible chain, thus it is valid to use physical model to extract DNA structural information.

The primal experiments on understanding DNA conformation are from X-ray crystallography. Watson and Crick discovered and confirmed the double helix structure of double strand DNA. They were jointly awarded with the 1962 Nobel Prize in Physiology or Medicine. After the development of fluorescence microscopy of single-molecule DNA in the last few decades, researchers were able to observe DNA by optical microscope which hugely pushed people's acknowledge. In the last decades, combining the nanofabrication technology, researchers are finally able to confinement DNA chain in a "slit" like trap. It can be treated as semi-2D confinement since there

is no restraint on x-y plane and confinement in z- direction. Reducing the dimensionality of the problem greatly simplified the physical problem. The are several important physical parameters describing the polymer chain. To understand these parameters is prerequisited since they can characterize the physical property of DNA chain.

1.3 Fundamental parameters of DNA

The most important parameters to characterize DNA include the DNA chain contour length, radius of gyration and the persistence length.

1.3.1 Contour length

The contour length represents the full length of polymer chain when it is stretched as a straight string. It is also defined as polymer's length at maximum physically possible extension. In terms of DNA chain, it can be simply calculated as:

$$L = N \cdot l \tag{1.3.1}$$

Where L is the contour length of polymer chain. N is the number of monomers composing the chain. l is the length of unit monomer.

1.3.2 Radius of gyration

Since not all of the polymer are in linear form, circular and branch form can not be characterize properly by contour length. Radius of gyration indicates the size of polymer. It is defined as the summation of distance between monomer and center of mass.

$$R_g^2 = \frac{1}{N}\sum_{i=1}^{N}\left(\overrightarrow{R_i} - \overrightarrow{R_{cm}}\right)^2 \tag{1.3.2}$$

Where R_g is the radius of gyration. N is the number of monomers. $\overrightarrow{R_i}$ is the position vector of i^{th} monomer. $\overrightarrow{R_{cm}}$ is the position vector of center of mass for the polymer.

$$R_{cm} = \frac{\sum M_i \overrightarrow{R_i}}{\sum M_i} \tag{1.3.3}$$

Assume all the monomers have the same mass. By substituting Eq.1.3.3 into Eq.1.3.1, we can get the general definition of radius of gyration. It does not depend the coordinate selection.

$$R_g^2 = \frac{1}{2N^2} \sum_{i,j}^{N} \left(\overrightarrow{R_i} - \overrightarrow{R_j} \right)^2 \tag{1.3.4}$$

1.3.3 Persistence length

Persistence length characterizes the polymer stiffness. The stiffness physically indicates the hardness to bend one polymer chain, or in the other word, the length one monomer needs to get rid of the impact from previous monomer. Persistence length depends on the intrinsic property of the bond between monomers. Thus, it is a characteristic parameter for different polymers.

For an ideal chain, two adjacent monomer will not affect each other. In this case, we can say the persistence length of this chain is 0. For an rigid bar(infinitely long), on the contrary, once the start point and orientation of the bar are known, we can simply claim the location of the rest pieces. In this case, we can say the persistence length is infinite long. Usually the real life polymers are in the situation in between. Two different monomers are correlated within some length then decorrelate beyond this limit. To clarify this point, we calculate the ensemble average of the square of

end to end length of polymer. The end to end length of polymer is defined as:

$$\overrightarrow{R} = \sum_{i}^{N} \overrightarrow{r_i} \tag{1.3.5}$$

Where $\overrightarrow{r}_i$ represents the position vector of i^{th} monomer. The ensemble average of the square of end to end length can be calculated as:

$$\left\langle \overrightarrow{R}^2 \right\rangle = \left\langle \sum_{i} \overrightarrow{r_i} \cdot \sum_{i} \overrightarrow{r_j} \right\rangle = \left\langle \sum_{i,j}^{N} \overrightarrow{r_i}\,\overrightarrow{r_j} \right\rangle \tag{1.3.6}$$

The orientation of i^{th} monomer can be defined as $\overrightarrow{t_i}$ and $|\overrightarrow{r_i}| = l$. Eq.1.3.6 can be further simplified as:

$$\left\langle \overrightarrow{R}^2 \right\rangle = l^2 \sum_{i,j} \left\langle \overrightarrow{t_i}\,\overrightarrow{t_j} \right\rangle \tag{1.3.7}$$

Where we can observe that $\sum_{i,j} \left\langle \overrightarrow{t_i}\,\overrightarrow{t_j} \right\rangle$ is a dimensionless number and this number indeed indicate the stiffness of polymer chain and it is named formally as tangent-tangent correlation function.

For semi-flexible chain, it is well known that the tangent-tangent correlation function should follow [15]:

$$\left\langle \overrightarrow{t_0}\,\overrightarrow{t_j} \right\rangle = \exp\left(-\frac{j}{P}\right) \tag{1.3.8}$$

And the parameter P is defined as persistence length. Persistence length indicates the correlation decay of the tangent vector along polymer chain. It can be interpreted as that after beyond the persistence length, we are not able to deduce any angle information of the previous monomer. For instance, two adjacent monomers must have very similar orientation since the bond between two monomers has limited degree of

freedom. Further are the monomers separating, the more degree of freedom will be accumulated. Beyond persistence length, monomer will not have any "memory" of the previous monomer.

By mathematical definition, the persistence length is defined as the length for tangent-tangent correlation function decays to e^{-1} of its maximum.

1.4 Microfluidics and Nanofluidics

Micro-nanofluidics is referred usually as the study to build up devices in order to conduct multi-purpose manipulation of small quantity liquid. Usually the liquid volume is in nano-litter to micro-litter scale. To achieve various functionality, embedded fine features are ubiquitous in those chips. Thus, micro-nanofluidics is an inter-disciplinary research area composed of physics, biology and engineering.

(Insert graph: length scale from nano-milimeter)

In the past few decades, the growth of micro-nanofabrication technology makes the micro-nanoscale fluidics precise control more accessible. By combing the electron beam lithography, chemical etching and bonding techniques, researchers can fabricate various structures ranging from micron scale to sub-nanometer scale[23]. Sophistically designed chips have various functionalities, such as cell culture[36], cell sorting[3], clinical diagnostic[35], DNA amplification[14] and so on. In particular, physicists take advantage of MEMS fabrication technology to build chip platform and characterize polymer behaviours. The fundamental study of how the polymer chain behaves in such a small length scale can unveil numerous great scientific interesting problems. DNA and proteins for example, are well known for importance in

biosystem, but how these bio-polymers are modulated by the environment is still a mystery since it is hard to isolate environment variables.

On the other hand, micro-nanofluidics devices provide researchers with the ability to change single variable while keep the rest unchanged. Ionic buffer, accessible space and different chemical interaction are the three most prominent aspects researchers are working on. In the work presented here, we focus on the space confinement in particular.

Polymer under confinement is one of the most vigorous studies based on fluidics chip. Researchers extensively change the accessible space of polymer chain(usually DNA) while other parameters remain the same. Depending on the confinement structure, two general types of confinements are categorized. Slit-like confinement(2D) serves as the main platform in polymer confinement experiment. slitlike confinement essentially applies confinement to polymer in one dimension while the left two dimensions are free. Nanochannel confinement(1D) applies confinement in two orthogonal directions while the translation dimension is free. In this study, we try to make the step further to a prototype of nanocavity(0D) confinement.

1.5 Overview of this work

My goal is to write this thesis in a self-contained way. The details of our experiments and how to understand our experiment results can be found in this thesis.

To begin with, DNA in slit-like confinement will be reviewed in Chapter 2. The theory, simulation and experiment results of slit-like confinement will be shown. This will provide a solid background of understanding how spatial confinement affects polymer behaviours. Further, by introducing cavity confinement in Chapter 3,

theories and several pioneering active confinement technologies will be reviewed. The structure and functionality of our fluidic chip will be discussed in the end. In Chapter 4, I will briefly show the fabrication method of our chip since my lab mate Xavier Capaldi has discussed it extensively in his thesis. I will focus more on our experiment setup and experiment protocol. In Chapter 5, experimental data and analysis will be shown in detail. Discussion will be made to give more physical insight of the problem. In Chapter 6, a brief conclusion will be given. *Chapter 5* and *Chapter 6* are from the paper on this project we published on Soft Matter[8]. In chapter 7, I will briefly show the current process of multiple chains interaction project. Preliminary data is given and position switching problem is proposed tentatively.

CHAPTER 2
Review of slit-like confinement

Slit-like confinement is one of the major platforms for DNA confinement experiment. Different from the nanochannel confinement confining DNA chain in both $x-$ and $y-$ direction, slit-like only confines DNA chain in one dimension. A vivid illustration of slit-like confinement geometry is shown in Figure 2–1.

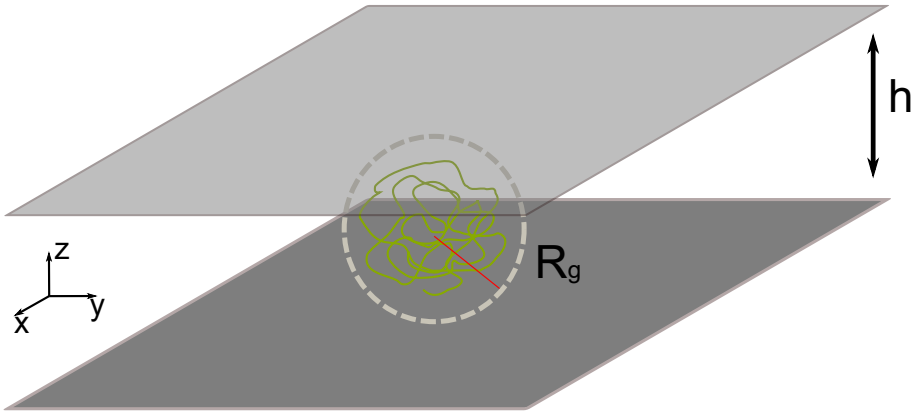

Figure 2–1: Schematic of slit-like confinement. The slit channel is formed by bonding an etched substrate with a flat cover. This schematic shows a slight confinement case when $h > 2R_g$

h indicates the height of the slit. Polymer chains in between can only travel in the slit defined by the floor and ceiling plane. On $x-$ and $y-$ direction, the slit wall is far enough from the polymer chain that wall-chain interaction can be neglected.

Polymer chain's behaviour strongly depends on the confinement height h, the radius of gyration R_g of the polymer chain and the persist length P of the chain. Historically, three confinement regimes have been assumed and experiments have been conducted extensively in the last few decades. Noted that R_g means the radius of gyration of polymer chain in *free standing solution*, which is called *bulk solution*, without further explanation.

When $h > 2R_g$, the confinement of the slit is near improbable and it is defined as ***Bulk regime***.

When $P \ll h < R_g$, polymer chain is compressed moderately. Blob model is composed by *Brochard and de Gennes* [7]. This regime is defined as ***de Gennes regime***.

As the confinement on $z-$ axis going further, the translational and orientational degree of freedom are restricted. When $h \sim< P$, *Odijk* [37, 38] proposed a sequence of theory to explain the conformation of DNA in such confinement. This regime thus is defined as ***Odijk regime***.

In the following section, a review will be provided in all of three regimes. I will review the theory, simulation and experimental works in slit-like confinement have been done so far. As theory may not be consistent with experiment, the discrepancy will be marked in the following discussion.

2.1 Bulk regime

In *Bulk regime*, the confinement from environment is so casual that polymer chain can not feel it. Thus, the conformation of the chain mostly depends on the effective repulsion between monomers and the entropy loss due to alignment of the

monomers of the chain. The balance between these two effects are approximately characterized by *Flory theory*. Flory theory describes the free energy of the polymer system by separating energetic and entropical parts. Then, the conformation of polymer can be found by minimize the free energy.

Consider a polymer chain with N monomers. Since the polymer tends to coiled up into a globule. The volume of polymer can be defined as R^3. Flory theory makes an assumption that the monomers are uniformly distributed if there is no interaction(correlation) between adjacent monomers. Suppose the concentration of polymer chain is sufficiently low, which is exactly the case in single molecular experiment. We have:

$$c = \frac{N}{R^3} \tag{2.1.1}$$

$$\lim_{c \to 0} \Pi = ck_B T \tag{2.1.2}$$

Where symbol Π represents the osmosis pressure. Without the monomer-monomer interaction, the probability density of finding the second monomer at any unit volume should be proportional to the concentration.

$$P\left(r, noncorrelated\right) \propto c \tag{2.1.3}$$

Since the polymer solution is dilute, the osmosis pressure can safely be approximated with ideal gas model. Further, if there is slight interaction between monomer, which is always the case in reality, the probability density of finding the second monomer at distance r should follow Boltzmann distribution, which is:

$$P\left(r, correlated\right) = c \exp\left[-\frac{U\left(r\right)}{k_B T}\right] \tag{2.1.4}$$

Thus, the interaction between monomers results in reduce of the accessible space, which is defined as the excluded volume v. It can be formulated as:

$$v = \int c - P\left(r, correlated\right) dr^3 = c \int 1 - \exp\left[-U\left(r\right)/k_B T\right] dr^3 \tag{2.1.5}$$

Combine Eq.2.1.1 and Eq.2.1.2 together and note that there are N monomers on a chain. We result in:

$$F_{energy} \approx N \Pi v = k_B T v \frac{N^2}{R^3} \tag{2.1.6}$$

Where v is defined in Eq.2.1.5. To calculate Flory estimation of entropy contribution in free energy, energy required to stretch a chain is evaluated. Note that stretching of a chain can be really difficult since the force can be hardly calculated on each monomer. To solve this problem, a new monomer unit larger than the Kuhn length needs to be constructed. The stretching thus can be treated as a perturbation based on the new monomer unit. The length of the new monomer unit is:

$$b_{new}^2 \approx b^2 g \tag{2.1.7}$$

Where b is Kuhn length, g is the number of monomers in each new unit. Obviously, right now there are N/g new monomer units in the chain. As the chain been stretched out, the end to end length of the length can be written as:

$$R \approx b_{new}\frac{N}{g} = \frac{Nb^2}{b_{new}} \tag{2.1.8}$$

By partition theory, reducing one degree of freedom results in $\frac{k_BT}{2}$ difference. The polymer chain is stretched out that 2 degrees of freedom is reduced. Further, since there are $\frac{N}{g}$ new units. We can estimate the entropical free energy as:

$$F_{entropy} \approx k_BT\frac{N}{g} \approx k_BT\frac{R^2}{Nb^2} \tag{2.1.9}$$

Thus, the total free energy of a real chain in Flory theory is the summation of Eq.2.1.6 and Eq.2.1.9:

$$F = F_{energy} + F_{entropy} \approx k_BT\left(\frac{vN^2}{R^3} + \frac{R^2}{Nb^2}\right) \tag{2.1.10}$$

We take the derivative of Flory free energy respect to the size of polymer R to retrieve R which can minimize free energy.

$$\frac{\partial F}{\partial R} = k_BT\left(-\frac{3vN^2}{R^4} + \frac{2R}{Nb^2}\right) = 0 \tag{2.1.11}$$

Solve the Eq.2.1.11 and set $v = b^3$, we result in:

$$R^* = Const \cdot v^{1/5}b^{2/5}N^{3/5} = Const \cdot bN^{3/5} \tag{2.1.12}$$

By refering Eq.1.3.7, we notice $\left\langle \overrightarrow{t_i} \cdot \overrightarrow{t_j} \right\rangle = 0$ unless $i = j$ in ideal chain case(no direction correlation between monomers). Thus, we get:

$$\sqrt{\left\langle \overrightarrow{R}^2 \right\rangle} = Const \cdot bN^{1/2} \tag{2.1.13}$$

It may seem ambiguous that the the size of polymer chain is defined with volume definition in Flory theory while in real chain case it is defined as the ensemble average of square root of end to end length square in ideal chain case. Actually, this definitions are the same but in different coordinate system.

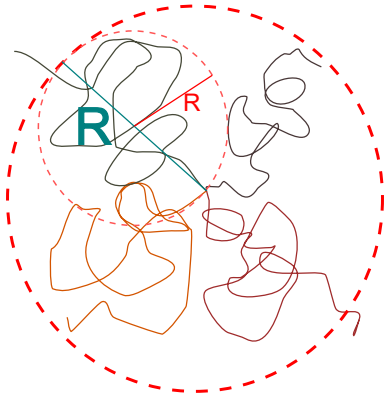

Figure 2–2: Relation between R and R_G.

Suppose we pin one side of all polymer chains from ensemble to origin. Obviously, the random orientation will cause $\left\langle \overrightarrow{R} \right\rangle$ vanish. Once we measure $\left\langle \overrightarrow{R}^2 \right\rangle$, since there is no correlation between monomers. As we have shown in Eq.1.3.2, R with volume definition is shown in Figure. 2–2 with red color. The cyan line indicate $\sqrt{\left\langle \overrightarrow{R}^2 \right\rangle}$. Thus, the ambiguity is clarified.

There is a great difference between ideal chain and real chain. The scale factor for monomer number N in real chain is larger than the ideal chain. It makes sense that the when the excluded volume is larger than 0, the adjacent monomers tend to depart away from each other.

The Flory theory has been validated by both experiments and simulations. More sophisticated theory, renormalization group theory for example, gives out comparable

result on this problem. However, Flory theory itself is problematic that it overestimates the energetic potential. By coincidence, this error is cancelled smoothly.

Flory theory is still useful. It gives out reasonable result with very simple formulism. Generating free energy by counting different contribution components is referred as "Flory theory" in this work without further notice.

2.2 de Gennes regime

In *de Gennes regime*, polymer is compressed moderately. The confined chains start feeling the dimension changing of the confinement. Be aware that de Gennes regime under slit-confinement is different from nanochannel confinement. F.Brochard and de Gennes[7] proposed a theory explaining the mechanism of polymer chain conformation in this regime with slit-like confinement. The theoretical scaling law matches the experimental results.

2.2.1 Chain conformation of de Gennes regime

Generally, there are two distinct methods can lead the scaling law in de Gennes regime. de Gennes[13] solved the problem by assuming the continuous changing between bulk regime and de Gennes regime. I will follow his method firstly to recover the scaling law.

Polymer chain under confinement $P \ll h < R_g$ is not isotropic. It expands with circular shape but pushed hardly on $z-$ axis. $\sqrt{\left\langle \overrightarrow{R}^2 \right\rangle}$ in bulk regime is abbreviated as R_{bulk}. The same quantity in de Gennes regime can be represented as $R_{deGennes}$.

Because we assume that the end to end length changes continuously and follows scaling law, we have:

$$R_{deGennes} = R_{bulk} \cdot f\left(\frac{R_{bulk}}{h}\right) = R_{bulk} \cdot f\left(x\right) \tag{2.2.1}$$

where the function $f(x)$ follows:

$$f\left(x\right) = 1, x \to 0 \qquad\qquad f\left(x\right) = x^m, x \gg 1 \tag{2.2.2}$$

By substitute Eq.2.1.12 into Eq.2.2.1, we can get

$$R_{deGennes} \sim N^{\frac{3}{5}(m+1)} b^{m+1} h^{-m} \tag{2.2.3}$$

A trick is applied here. Now we confine our chain on a plane uniaxially. For 2D problem, Flory theory is still valid by changing the polymer concentration! Flory theory constructs the free energy by energetic term and entropy term. It does not prerequisite 3D space. The concentration of monomer in 2D can be calculated as $\frac{N}{R^2}$. Thus, the "2D bulk regime" will result in scaling relation:

$$R_{bulk,2D} \sim N^{3/4} \tag{2.2.4}$$

By matching above relation with Eq.2.2.3, we can easily find m can only be $\frac{1}{4}$. Thus we get the following relation:

$$R_{deGennes} \sim N^{\frac{3}{4}} b \left(\frac{b}{h}\right)^{\frac{1}{4}}, (for R_{bulk} > h) \tag{2.2.5}$$

For the second method, the Flory theory can resolve the same result by making an argument on the both terms. The exclusive space, in 2D case is $\sim h^2$. The coarse-grain idea applies here again. We combine several Kuhn monomers in a way

that the new unit will not correlate with the adjacent new unit. Suppose that there are g Kuhn monomer in one new unit. The number of new coarse-grained monomers can be defined as:

$$N_{coarse} = \frac{N}{g} \tag{2.2.6}$$

The end to end length of the chain is still represented with $\overrightarrow{R}$. The energy term and entropy term can be modified with the new coarse-grain unit.

$$F^*_{energy} = k_B T h^2 \frac{(N/g)^2}{R^2_{/\!/}} \tag{2.2.7}$$

$$F^*_{entropy} = k_B T \frac{R^2_{/\!/}}{(N/g)\, h^2} \tag{2.2.8}$$

Thus the modified Flory free energy is:

$$F_{deGennes} = k_B T \left(h^2 \frac{(N/g)^2}{R^2_{/\!/}} + \frac{R^2_{/\!/}}{(N/g)\, h^2} \right) \tag{2.2.9}$$

Thus by minimizing Flory free energy with respect to end to end length, we can resolve the result in Eq.2.2.5.

2.2.2 Dynamics of de Gennes regime chain

The dynamics of polymer chain can be estimated by Einstein relation directly. Einstein relation is obtained by modeling sphere instead of polymer chain. However, by estimating the motion of chain center of mass, the dynamics of chain can be

estimated. The Einstein relation is shown as:

$$D = \frac{k_B T}{\zeta} \tag{2.2.10}$$

Where D is the diffusion constant, ζ is the friction constant of particle. The diffusion model is built on sphere, but it can be generalized by finding the effective friction constant of polymer chain.

Different from a rigid sphere, the internal freedom and constrain of polymer chain can affect the dynamics of chain greatly. If we can analyse interaction between every possible pairs of monomers, the problem can be solved approximately by Newtonian Mechanics. It is obvious that this approach is prohibited greatly by the large number of chain internal freedom and the Brownian fluctuation on each pair. This problem can not be solved numerically if multi-interaction is taken into account.

Coarse-grain method, on the contrary, provides a simple formulation which reveals the scaling directly. This is remarkable. Coarse-grain assumed that the monomers inside a blob can not feel any confinement. The grained blob with the size equal to the slit height. This sequence of blobs will do a self-avoid walk in 2D. This difficult problem is solved by combining solution in two different dimensions! At the first step to the solution, the problem rises naturally. How many monomers(Kuhn units) are inside one blob?

By referring Eq.2.1.12, the R^* should be equal to slit height h since the blob has the same size of slit. By solving N, we can estimate the scaling of number of Kuhn monomers in one blob and it is represented here as g.

$$g \sim h^{5/3} b^{-5/3} \tag{2.2.11}$$

Noted that Kuhn length is equal to persistent length p since there is no correlation between Kuhn monomers. Also, it is assumed that there is no drain from adjacent blob. After coarse-graining the original chain, the blob chain should follow de Gennes relation shown in Eq.2.2.5. Thus, we can replace all the parameters by after coarse-grain parameters. Notice that

$$N = N_{blob} \cdot g \tag{2.2.12}$$

$$b \sim hg^{-3/5} \tag{2.2.13}$$

Plug the relation above into Eq.2.2.5 and result in:

$$R \sim hN_{blob}^{3/4} \tag{2.2.14}$$

Considering the friction constant of the chain:

$$\zeta_{chain} \sim \zeta_{blob} N_{blob} \sim \eta h \left(\frac{R_G}{h} \right)^{4/3} \tag{2.2.15}$$

R_G is the 2D radius of gyration of chain under confinement. It is defined as the projection of 3D R_G on $x - y$ plane.

Thus the diffusion constant in de Gennes regime should follow:

$$D \sim \eta^{-1} h^{-1} \left(\frac{R_G}{h} \right)^{-4/3} \tag{2.2.16}$$

In addition to diffusion constant, the relaxation time is the second quantity characterizing the polymer chain dynamics. The relaxation time reflects the intrinsic elasticity for polymer.

The elastic force required to stretch a chain for dR has been proved that:

$$F_{elastic} = -\frac{k_B T}{R^2} dR \tag{2.2.17}$$

The drag force from the adjacent solvent particle should be proportional to the rate of length change. Thus, the drag force can be shown as:

$$F_{elastic} = -\frac{k_B T}{R^2} \delta R \tag{2.2.18}$$

On ensemble average, the elastic force should balance the drag force. Thus, we have:

$$\delta \dot{R} = -\frac{k_B T}{\zeta_{drag} R^2} \delta R \tag{2.2.19}$$

Assuming the size of the chain is a constant over time. The solution of the above equation is simply an exponential function. Noted it is a solution for δR, not R. The decay time τ is defined as:

$$\tau = \frac{\zeta_{drag} R^2}{k_B T} \tag{2.2.20}$$

Assume that the hydrodynamics is dominant in drag constant. By plugging Eq.2.2.15 and chain size in Eq.2.2.20, we can reach the following scaling relation:

$$\tau \sim h^{-\frac{7}{6}} N^{\frac{5}{2}} b^{\frac{25}{6}} \tag{2.2.21}$$

2.2.3 Experiments in de Gennes regime

The de Gennes blob theory is constructed based on the assumption that there is no drain between the adjacent blob. In reality, the blob with size the same as the

slit height might still has in and out flux of Kuhn monomers. This effect makes the scaling relation is slightly weaker than the predicted value.

As presented in Stein's work [45], they notice the diffusion constant scales proportional to $h^{\frac{2}{3}}$ when $h < R_G$. The parameter R_G here is the 2D radius of gyration under confinement. In Stein's work, he eliminates R_G in Eq.2.2.16 by substituting Eq.2.2.5 in. Notice that N and b in his study are constants since he uses the same species of chain. Thus, the theoretical scales matches his experiment. The probing regime thus is in de Gennes regime.

Another work is even more convincing. Balducci et al [1] did multiple experiments on different length DNA samples. DNA chains with different lengths follow the scaling relation, but with slightly smaller value. In theory, the predicted scaling value is $\frac{2}{3}$ while in his experiment, it is about 0.45 to 0.55.

Beyond the diffusion constant scaling, the relaxation time scaling is validated by experiment. Hsieh et al [22] conducted experiment measuring the DNA chain rotational relaxation time for different slit heights. The relaxation time τ is proportional to $h^{-0.92}$, which did match $\tau \sim h^{-\frac{7}{6}}$ in Eq.2.2.21 closely.

It is quite interesting that the absolute value of scaling factor for both dynamic quantities are smaller than the theory. This was explained further by building up a new polymer describing model. The theory shown above is named as "Zimm-blob" system. The essential assumption of Zimm-blob is that there is no drain between blobs, thus the adjacent blobs are not correlated. There is another type of blob model. Instead of a sequence of uncorrelated blobs, the chain is modeled by blob-spring-blob structure. The adjacent blobs are correlated via a harmonic potential.

This model is named as "Rouse-blob". From the experiments result, they tempt to conclude that the DNA chain is actually between Zimm-blob chain and Rouse-blob chain. This means DNA chain does form blobs, but the Kuhn monomers can transfer from one blob to the other one.

2.2.4 Simulations in de Gennes regime

Y.L.Chen has presented a Brownian dynamics method with hydrodynamic interactions(BD-HI) simulation and confirms that the scaling law in de Gennes regime is valid[9]. The principle of the simulation is shown in

$$d\overrightarrow{R} = \left[\overrightarrow{U} + \frac{1}{k_B T}\mathbf{D}\cdot\overrightarrow{F} + \nabla\cdot\mathbf{D}\right]dt + \sqrt{2}\mathbf{B}\cdot d\overrightarrow{W} \tag{2.2.22}$$

where dt is the time step. $\overrightarrow{R}$ is the position of monomer on the chain. $\overrightarrow{U}$ is the flow velocity field without perturbation from the chain. $\overrightarrow{F}$ is the force applied on current monomer. $d\overrightarrow{W}$ is a Brownian fluctuation. $\mathbf{D} = \mathbf{B}\cdot\mathbf{B}^T$ is a $3N \times 3N$ diffusion matrix[9]. By calculating the time evolution of each monomer, they are able to extract both the DNA conformation and diffusion constant.

The scaling relation calculated from theory Eq.2.2.5 between the size of DNA and slit height is in agreement with simulation. Moreover, the diffusion constant scaling relation is validated by the simulation again.

2.3 Odijk regime

When the slit height is smaller than the persistence length, the blob conformation of the DNA chain will vanish. The limited accessible space leads the chain to elongate by successive deflections from the floor and ceiling. According to the physical picture, the chain dynamics and conformation should change greatly at the

transition point between de Gennes and Odijk, but latest experiments show that there are discrepancies between experiment and theory.

2.3.1 Theory of polymer in Odijk regime

Odijk's theory has two separate branches. The branch in nanochannel confinement has a great success. However, it is still a debating problem in slit-like confinement. Even the existence of Odijk regime in slit-like confinement is not clear. Here, I will briefly review the Odijk theory in nanochannel confinement and point out the contradiction in slit-like confinement.

The initial formulation in nanochannel confinement is quite simple. Yamakawa[56] has shown the semi-flexible chain(like DNA) in bulk follows the relation:

$$\left\langle \overrightarrow{r}^2(x) \right\rangle \simeq x^2 \left[1 - \frac{x}{3P}\right] \tag{2.3.1}$$

$$\left\langle \left(\overrightarrow{r}(x) \cdot \overrightarrow{u}(0)\right)^2 \right\rangle \equiv \left\langle \overrightarrow{z}^2(x) \right\rangle \simeq x^2 \left[1 - \frac{x}{P}\right] \tag{2.3.2}$$

Where x means the contour distance from the start point of the chain. Noted that he assumes the first rigid rod align with $z-$axis in the derivation. Thus, the mean-squared deviation from $z-$axis can be noted as:

$$\left\langle \varepsilon^2(x) \right\rangle = \left\langle \overrightarrow{r}^2(x) \right\rangle - \left\langle z^2(x) \right\rangle = {}^{2x^3}\!/_{3P} \tag{2.3.3}$$

Odijk[37] uses a very sample notation to approximate the condition when the polymer is firmly confined in a tube,where $D \ll P$.

$$\left\langle \varepsilon^2(x) \right\rangle \simeq \left(\frac{1}{2}D\right)^2 \tag{2.3.4}$$

$$\lambda^3 \simeq D^2 P \tag{2.3.5}$$

Thus, the behavior of small fractions with length λ of the chain is very similar to a rigid rod.

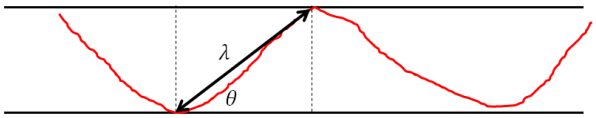

Figure 2–3: Schematic of a polymer chain confined in nanochannel in Odijk regime. The small fraction of the the polymer can be treated as a rigid rod and the polymer is deflected by the walls of channel.

The end to end length of a chain can be calculated as:

$$R_{odijk} = N\lambda\cos(\theta) = L\left(1 - \frac{1}{2}\theta^2\right) \sim L\left[1 - A\left(\frac{D}{P}\right)^{\frac{2}{3}}\right] \tag{2.3.6}$$

Where N is the number of fractions in the polymer. L is the contour length of the polymer chain. A is a numerical constant depending on the channel geometry. For a cylindrical channel, $A \approx 0.17$. For a rectangular channel, $A \approx 0.18$.

The free energy increase due to the confinement can be calculated in a sample way. Odijk[37] suggests that any polymer fraction shorter than λ can be treated as a rigid rod. Since the free energy should be an extensive quantity, the free energy has to be proportional to $\frac{L}{\lambda}$. Thus, the following arguments can be made:

$$\Delta F_c = Ck_BT\frac{L}{P^{\frac{1}{3}}D^{\frac{2}{3}}} \tag{2.3.7}$$

Note that the polymer contour length has to be much longer compared with the persistence length and the rigid rod length has to be much smaller than persistence

length. C is a geometric constant again. For a rectangular nanochannel, the aspect ratio of channel should be taken into account for the free energy increase.

2.3.2 Experiment in Odijk regime

Many existing nanochannel confinement experiments try to probe the polymer conformation in both Odijk regime and the transition phase between de Gennes regime to Odijk regime. Note that the de Gennes regime mentioned here is in nanochannel confinement. The slit-like confinement de Gennes regime theory has been reviewed previously.

Typically, the nanochannel is defined by electron beam lithograph(EBL) method in fused silica substrate. Thus, the top-down fabrication method usually results in rectangular shape channel. The DNA chains are driven inside the nanochannel either by pneumatic pressure or electrophoresis depending on the channel cross-section. After DNA chain entering the channel, considerable thermal fluctuation can change the chain conformation continuously. By analysing the extension length and the relaxation time of DNA chain in nanochannel, we can extract the conformation and dynamic information of chain.

Reisner et al[41] has measured the extension length of DNA with different effective channel widths from $400nm$ down to $30nm$. The DNA extension data follows power scaling law at large channel width by de Gennes theory, but has obviously smaller chain extension at around $30nm$ width, which indicates the Odijk regime. This shifting point actually matches the prediction from Odijk nanochannel confinement theory. Besides, DNA extension from $30nm$ up to $100nm$ can be fitted by Odijk theory well. Further, they measured the DNA chain relaxtion time and observe a

strong peak at around $150nm$. Thus, they conclude that the onset of Odijk regime is around $2P$. Several following works[49, 53, 40] later confirmed the DNA extension measurement.

Not like the experiment in nanochannel, the slit-like confinement experiments are quite ambiguous. Both Balducci[1], Strychalski[46], Tang et al[48] and Cifra et al[11] observed the DNA dynamics and conformation under nanoslit confinement environment. Interestingly, none of them observed drastic diffusion constant change at the onset of Odijk regime($\sim 2P$). On the contrary, Lin et al[33] has observed extension scaling change approximately at $100nm$, which matches Reisner's experiment in nanochannel. In simulation point of view, Dai et al[12] and Tree[50] give out simulation results showing that the Odijk regime in nanoslit does exist. The transition is gradual and there are many subregimes within Odijk regime existing.

2.3.3 Summary

Although it seems like physicists have built up a systematic framework for DNA confinement problem, more contradictions between experiment and theory are found in transition regimes from de Gennes regime to Odijk regime and de Gennes regime to Bulk regime.

For transition from Bulk regime to de Gennes regime, Bonthuis[4] and Uemura[51] observed the size of DNA chain, either radius of gyration or major extension length, initially decrease with the slit height going down until $\frac{R_{G,bulk}}{2}$. On the contrary, Lin[33] and Tang[48] observed the DNA size increases monotonically with the slit height decreasing. The simulation results at the transition regimes also have some conflictions.

Odijk theory in slit-like confinement is not as clear as de Gennes theory. As we discussed in previous section, the experiment on probing transition from de Gennes regime to Odijk regime in slit confinement all show a gradual scaling change instead of a abrupt changing. Theories tend to subdivide Odijk regime into many subregimes while the transition between regimes are continuous. More works are needed to complete the study in ultrathin slit confinement.

CHAPTER 3
Device fabrication

The fluidics device is fabricated by top-down method. Combining different lithograph technology, etching and bonding techniques, we are able to fabricate a free-standing membrane above the main fluid chamber which can be actuated dynamically. Different from the conventional PDMS fluidic device, our device is bonded anodically with silicon substrate. It provides two great advantages over PDMS device. First, the Si substrate is used as the supporting structure of the device. As an inorganic crystal wafer, the embedded channel can be cleaned by standard microfabrication clean protocol. Thus, the fluidics channel environment is more controlled. The second advantage is that the Si substrate is not fluorescent generically. It will increase the signal-noise ratio. Polydimethylsiloxane(PDMS), however, can bind with various fluorescent dyes which will apply a time dependent fluorescent background in experiment. Free standing membrane structure also makes coupling fluidics with other nanoscale features possible. It provides a robust platform to study nanoscale dynamics on single molecule level.

My colleague Xavier Capaldi has written a detailed fabrication review on varies fabrication technologies in fluidic device in his thesis. Hence, I will present the fabrication flow of our device without further exploring the technology.

3.1 Device overview

The device is a two-layer stack. The fluidic channel and nanocavities are etched upon the borosilicate substrate. Low stress silicon nitride membrane(LS SiNx) is coated on 4-inch silicon wafer by low-pressure chemical vapor deposition(LPCVD). Two substrate wafers are bonded anodically. After bonding, we etched multiple access ports on the top side of silicon wafer. Free-standing silicon nitride membrane thus is formed at the interface between two substrate.

3.2 Fabrication flow

The fabrication procedure is shown below:

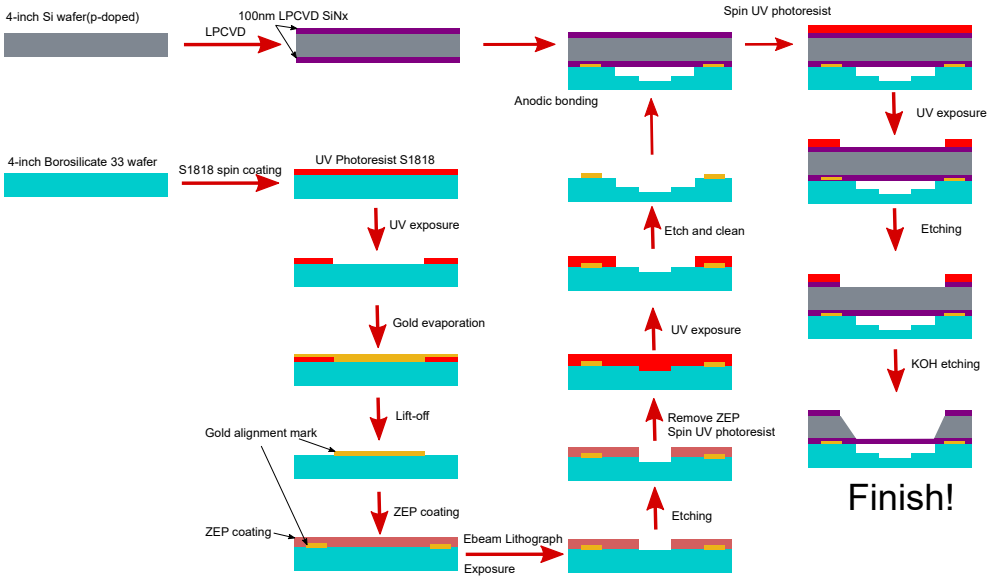

Figure 3–1: Device fabrication flow. Both UV lithograph method and E-beam lithograph method are applied in borosilicate substrate fabrication. Grey silver blocks represent silicon substrate. Light blue blocks represent borosilicate substrate. Purple layer represents SiNx membrane. Red layer represents UV photoresist S1818. The dark red layer represents E-beam photoresist ZEP 520A. Gold alignment mark is made by a lift-off process and used to align cavities, channels and top access ports together.

We start our fabrication process with two plain substrates. For etching across wafer uniformity and bonding quality, we chose 4-inch as our primary wafer size. We have three masks in total and all of these masks are aligned together. The alignments mark and global lines are printed on one mask and named as alignment mask. Micro loading channels are printed on the second mask and named as channel mask. The topping loading ports are printed on the third mask and named as ports

mask. Alternatively, if the critical features are more than $3\mu m$, the fine features can be printed on the fourth mask. In our case, to achieve the geometry accuracy, our nanocavities are defined with E-beam lithograph. In following section, I will explain the fabrication of silicon wafer and borosilicate 33 wafer separately.

3.3 Silicon wafer fabrication

The silicon nitride film is fabricated in Cornell NanoScale Science and Technology Facility(CNF). The starting thickness of silicon wafer is $400\mu m$. The silicon wafers are p-doped to meet the requirement of anodic bonding[31]. Wafer surface is Si $< 100 >$ plane. Both sides of the wafer are polished before LPCVD silicon nitride coating.

Since pneumatic pressure will be applied to the membrane, the thickness and stress of the membrane is extremely critical in our device. To optimize the membrane thickness, we did experiment on both $50nm$ and $100nm$ device. The result indicates that membrane with either thickness can be pressed to the glass floor of fluidics channel easily.

Further, the membrane deflection can be modeled with following equation:

$$w_0 = 0.318 l^3 \sqrt{\frac{ql}{Eh}} \tag{3.3.1}$$

Where w_0 is the maximum deflection, l is the membrane width, q is the loading pressure, E is the Young's modulus and h is the membrane thickness.

In our device, the membrane width is around $50\mu m \sim 100\mu m$. The pressure we use in experiment is around 3000mba. Thus, by substituting the number above into Eq.3.3.1, we reach the result that membrane can deflect to tens of micrometers!

This is pretty remarkable since we only has our channel in hundreds of nanometer. Thus, the membrane with $50 - 100nm$ can be pressed easily to the bottom channel.

Silicon nitride membrane is deposited by chemical vapor deposition(CVD). By controlling the input gas ratio, different types of silicon nitride film can be made. The principle reaction is shown as follow:

$$SiCl_2H_2 + NH_3 \rightarrow Si_xN_y + HCl + H_2 \tag{3.3.2}$$

Standard stoichiometric Si_3N_4 membrane film is deposited by controlling the ratio $SiCl_2H_2$:NH_3 = 1:5. By revising the input flow ratio up to 1:10, silicon-rich nitride film can be deposited. Also the temperature and flow pressure present as a dominant parameter in the final deposition result. In our case, we grow non-stoichiometric low stress SiN_x membrane by standard CNF recipe without exploring the huge parameter space.

3.4 Borofloat wafer fabrication

Nanocavities and microchannels are etched into the borosilicate glass wafer. To meet the need of anodic bonding, either Borofloat 33 or Corning Pyrex 7740 can be used. These two types of glass have very similar composition but from two distinct companies. They are interchangeable with each other in anodic bonding. In our case we use Borofloat 33 wafer. The glass is doped with B_2O_3 and Na_2O. These dopants can provide O^- to help bonding. More important, the thermal expansion coefficient of the listed glass substrate is comparable with Si wafer. It is important because the coefficient mismatch can cause bonding failure or crack of substrate. Our starting

borofloat wafers are provided by WaferPro Inc. The glass thickness is 200μm and the surface average roughness is below 4 angstrom.

3.4.1 Alignment marks lift-off

Gold alignment mark are transferred to glass substrate by standard lift-off process. All three lithograph steps are aligned with gold marks. Thus, the quality of lift-off is essential in our case.

Before starting the process, glass wafer is cleaned by acetone and IPA to remove all the residue ,particles and absorbed water. Asher clean is applied right before the coating to make sure no organic contamination is on the substrate surface.

After surface clean, diluted HMDS is spun on glass to improve the photoresist glass adhesion. We spin HMDS for 2min with 4000rpm. A pre-spin is conducted for 15s with 500rpm. After spinning, substrate is baked with 105 °C for 2min. Noted that the HMDS must be diluted to the correct concentration such that it will not crosslink with the photoresist. The crosslink may result in the photoresist development failure. Some microfabrication facilities provide an oven to vaporize HMDS and coat the substrate in low-pressure. The oven is preferred since it can coat a uniform thin layer across the entire wafer.

S1818 Microposit photoresist is applied right after the HMDS baking. We spun photoresist with 4000rpm for 2min. This spinning speed usually result in photoresis thickness between 1.5-2 μm. Baking is required after the spinning. We bake our coated substrate with 115°C for 90s. It will dehydrate the photoresist thus to prevent deformation after exposure and development. It also softens the photoresist a little bit and redistributed the photoresist to result in better uniformity. In both case,

baking after spinning is a required standard step in order to get desired lithograph result.

UV exposure is conducted after the photoresist coating. We use chromium hard mask in this project. The chromium mask is written by FrontRange Photomask Inc with laser writing technology. Maskaligner EVG-601 allows several modes for alignment. We use softcontact mode for the gold alignment mark. Constant exposure dose is chosen according to the machine. We use $200mJ/cm^2$ in our case. This dose may vary depending on the machine calibration of different facilities. For the transparent substrate, the UV reflection from the substrate may result in a "Zig-Zag" shape on the photoresist wall. To overcome this problem, a post-exposure baking(PEB) is required. The photoresist will be soften a little bit that the wall will become smoother. The internal stress of photoresist will reduce. PEB can also is typically performed at 110°C for 1-2min on a hotplate. Following the PEB, development will remove the exposed photoresist to form desired pattern. We develop our substrate with MF-319 for 60s while we manually agitate the beaker constantly. We check our sample carefully after the development. All the alignment features need to be transferred properly on the photoresist.

E-beam evaporation is used to deposit gold to our substrate. The adhesion between gold and glass substrate usually is not robust enough. We firstly deposit $5-10nm$ chromium as the intermediate layer. The deposition rate we use is approximately $1-2\mathring{A}/s$. Higher deposition rate may result in metal cracking. We fabricate 50nm thick gold alignment mark for the later process.

The chemical we use to do lift-off process is Microstrip-1165. We heat the solution up to 65°C and soak our substrate in solution for $1hr$. Sonication is forbidden since it will easily cause the depletion of metal layer. To remove the floating gold, we transfer our sample to a beaker contain IPA. After agitating the beaker gently for 1-2min, we carefully remove our sample out of the beaker and use nitrogen gun to dry the sample. Noted that the floating gold can easily adhere and redeposit on the substrate. The floating gold has to be dumped before wafer transfer. After the lift-off, we should be able to observe the gold mark clearly. Some gold alignment marks are shown in Fig .3–2

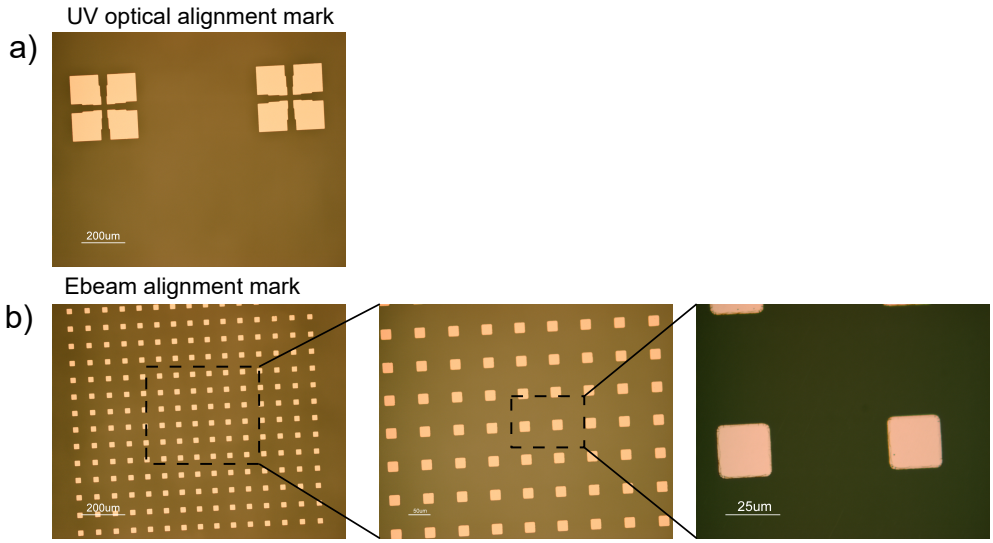

Figure 3–2: Gold alignment marks made by lift-off process. a) Alignment marks for UV lithograph. b) EBL alignment mark. The squares are in slightly different size to allow system auto-adjusting the orientation of wafer.

3.4.2 Nano-cavity fabrication

If the feature size is less than $2\mu m$ or the feature geometry is very crucial in application, EBL will be the ideal choice. EBL directly writes on photoresist by electron beam. Depending on the system, EBL can reach sub-10nm resolution. The cavity features can either be fabricated with standard UV lithograph method or EBL method depending on the critical size. The UV lithograph procedure will be the same as the introduced previously. Here I will briefly show EBL method.

ZEP-520A is a standard positive photoresist for Electron Beam Lithograph(EBL). The spinning protocol of ZEP-520A photoresist can be easily found online. The thickness of photoresist depends on the application needs. Typically, the thickness of ZEP520A is around $100-700nm$. A known fact is that spinning more than $400nm$ ZEP-520A can be problematic. More, dilution is required to reach a low thickness. For our device fabarication, we always spin twice of the critical feature depth to compensate the plasma etching in later step. The spinning starts with 300rpm for 3sec to spread the photoresist out. After pre-spin, the spinner reached desired speed and spin for 120sec. The desired spinning speed depends on aimming thickness. Baking is essential after spinning for the same reason as UV photoresist. 180°C 3min baking is ideal for ZEP-520A.

ZEP-520A can absorb electron and the charge accumulation effect can distort the writing electron beam. Undesirable defect forms if the charging effect happens during the exposure. To reduce the charging affect, we coat the wafer with $20nm$ chromium layer. Both the sputter and metal evaporation can deposition chromium. The metal evaporation is preferred in this process. During sputter process, X-ray can

be generated when the plasmons hit the metal target. X-ray will expose small amount of ZEP-520A easily. Thus, for deep feature EBL, metal evaporation is required.

The highly accurate features are designed on Tanner L-edit software. The actual EBL is conducted by the technician in Institut national de la recherche scientifique(INRS) Energie materiaux telecommunications research centre. The alignment is automatically carried out by the EBL software with the gold alignment mark. After exposure, we apply standard chromium etchant to remove the chromium layer. Since we only have $20nm$ thin chromium layer, the ZEP-520A photoresist mask is stable enough to survive the chromium etching. The entire etching takes approximately 30s. ZED-N50 is used to develop the photoresist after chromium etching. ZEP-520A is a highly sensitive photoresist, after exposure, 65s development can easily remove the exposed photoresist. IPA rinsing is applied after development to remove developer residue. Noted that IPA can also form residue if the IPA droplets are dried upon the photoresist. Thus, IPA needs to be blowed off the wafer completely and quickly. A typical ZEP-520A feature geometry is shown below in Figure.3–3:

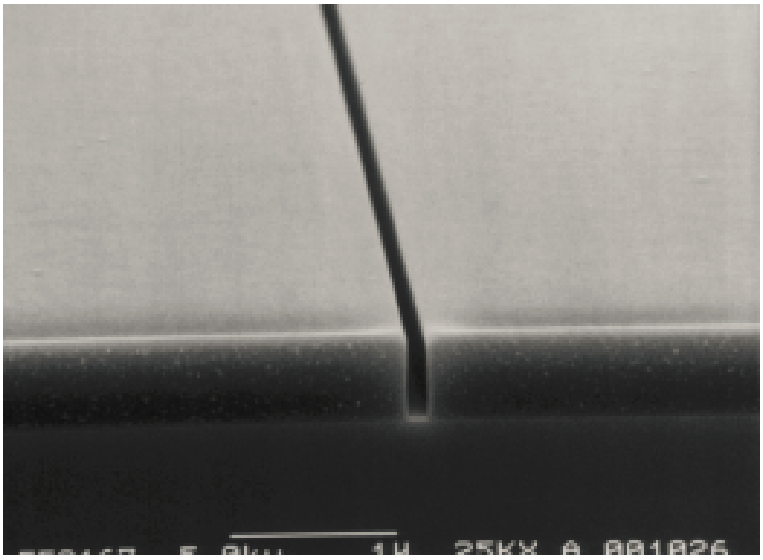

Figure 3–3: Example of ZEP-520A made feature. The photoresist is $500nm$ thick and feature width is $150nm$. Baking temperature is 180°C. Baking time is 2min. The exposure dose is $50 \times 10^{-5} \mu C/cm$. This example can be found in technical report of ZEP-520A from ZEONREX Electronic Chemicals.

Reactive ion etching(RIE) is a method to remove target material anisotropically. Usually the substrate is coated with a patterned mask so that the substrate without masking material will be etched. In our case, photoresist is the mask we use to transfer our nanofluidic features on glass substrate. The mechanism of RIE is to ionize reactive gas with high voltage RF field and bring reactive gas to the substrate surface by voltage drop between RF source and sample stage. The reactive ions can bind with the volatile components on the surface and removed by exhaust system. Not as easy as it sounds like from its mechanism, there are many etching parameters

Parameter	Value
ICP	2000W
Substrate power	150W
Argon	50sccm
SF6	5sccm
Pressure	<2mTorr
Temperature	20Celcius

Table 3–1: Parameter of Reactive Ion Etching process. Etching roughness in average is less than 10% of the etching depth.

and various etching principles in RIE process. The process needs to be optimized for specific task. It is not a trivial to tune the protocol until it works for the application.

In our case, the dopants in borofloat substrate behave as undesired mask to the volatile glass composition. The pure chemical etching results in a rough etched surface which is not desired in nanofluidics. To overcome the roughness, we apply inert gas(Argon) components to raise the power of physical etching up and remove the material more uniformly. The drawbacks of this physical etching is the sample can be heated up by the ions bombarding to a point that the photoresist is burnt. Moreover, the photoresist may even be unsuitable for physical etching since etching selectivity is lower than normal chemical etching. We coat ZEP-520A twice the depth of etching feature to solve the selectivity problem. The smooth etching of borofloat glass is still a engineering research topic[57]. The etching parameters are listed in table.3–1

With the etching parameters above, we are able to achieve a desired etching result. A typical cross-section roughness profile is shown as follow. The etching rate this protocol for borofloat is around $0.5 - 1\mu m/min$. The etching rate varies

depending on the size of feature and the depth of feature. The etching rate drops with the deeper features. Also the uniformity at the cross-section will drop as the features being etched deeper. Average roughness of this protocol in our application is around $5-10nm$. This roughness is acceptable since it is smaller than 10% of our feature depth.

3.4.3 Loading micro-channel fabrication

The nanofluidics cavities are etched into the glass first. The loading channels are etched after. While the channels are being etched, the cavities will be etched again. Fig.3–1 shows the order of two etching steps. Channel etching must be conducted after the cavity etching because ZEP-520A photoresist is only $200-400nm$ thick in total. ZEP-520A will not conform with the substrate surface properly if $400nm$ channels are etched in the substrate. With our etching flow, the UV photoresist is able to cover the entire surface since its thickness is usually between $1-2\mu m$, which is thick enough compared with $100-200nm$ deep cavities. The patterning of loading channel with UV photoresist is exactly the same as we use for gold alignment mark. After development, channels are etched with the same recipe as we etch the cavity features. The channels are aligned with the features so that the cavity features sit right in the middle of the channels.

3.5 Anodic bonding

The substrate is cleaned thoroughly with acetone and IPA after features/channels etching. The next step is to bond the silicon/silicon nitride wafer with glass substrate anodically. The anodic bonding requires a particle free surface. Any organic particle

Parameter	Value
Temeprature	350Celcius
Heating time	1hr
Bonding voltage	1000V
Bonding time	10min*3
Cooling method	Air cooling
Cooling time	3hrs

Table 3–2: Parameters of anodic bonding in our process. The substrate is heated up in 1hr precisely. We apply high voltage for 3 times in a row. In each time, the applied voltage is 1000V and kept for 10min. The substrate is cooled down naturally. Substrate can reach around 50 celcius after 3hrs cooling.

or dust can form a bubble at the wafer interface and will weak the bonding strength. We use piranha solution to clean both wafers right before the bonding process.

Heating, bonding and cooling are the three most important stages in anodic bonding. By heating phase, both substrates will be heated up to 350°C. The high temperature will improve the mobility of ions in both substrates. The actual bonding happens during bonding phase.The high voltage is applied to the anode and cathode electrode plate. The voltage will drive the mobile ions in substrate to the interface. The silicon wafer is p-doped, thus the positive dopants will move to the substrate interface. The O^- in borofloat substrate will move to the interface by the same mechanism. Two kinds of opposite ions will bind in pair that bond two substrate together without any intermediate adhesive layer.

The heating and cooling phase is vulnerable to thermal expansion coefficient mismatch between two substrate material. Even a slight mismatch will result in bonding failure. Borofloat 33 and Corning Pyrex 7740 both work fine for 4-inch

Si-glass with our bonding parameters. For lager wafer, heating and cool time needs to be optimized for the performance. A bonded wafer is shown in the Fig.3–4.

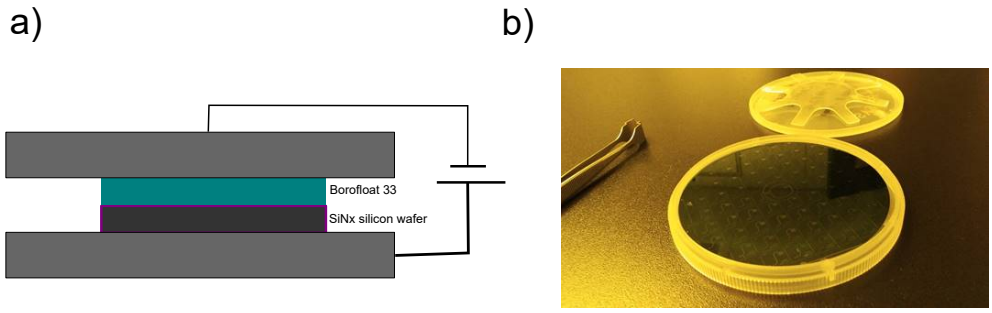

Figure 3–4: Bonding schematics and bonded wafer stack. a) shows a schematic of bonder. The cathode and anode are made of graphite plates. b) shows a bonded silicon-glass stack. We use SUSS SB6e Bonder in our project.

3.6 Backside alignment and KOH etching

We use the silicon nitride membrane as a hard KOH mask in our fabrication. Silicon nitride is extremely resistent to KOH etching(almost 0)[55].The silicon nitride on the top needs to be patterned before wet etching. A soft photoresist mask is pattern by UV lithograph first and KOH window is transferred to silicon nitride by standard CF4/CHF3 RIE etching.

The actual KOH mask window has to be larger than the desired membrane size. KOH solution only etches the 100 and 110 plane of silicon. The etching rate for 111

plane is nearly negligible. A convenient tool to calculate the KOH etching rate can be found here[1] .

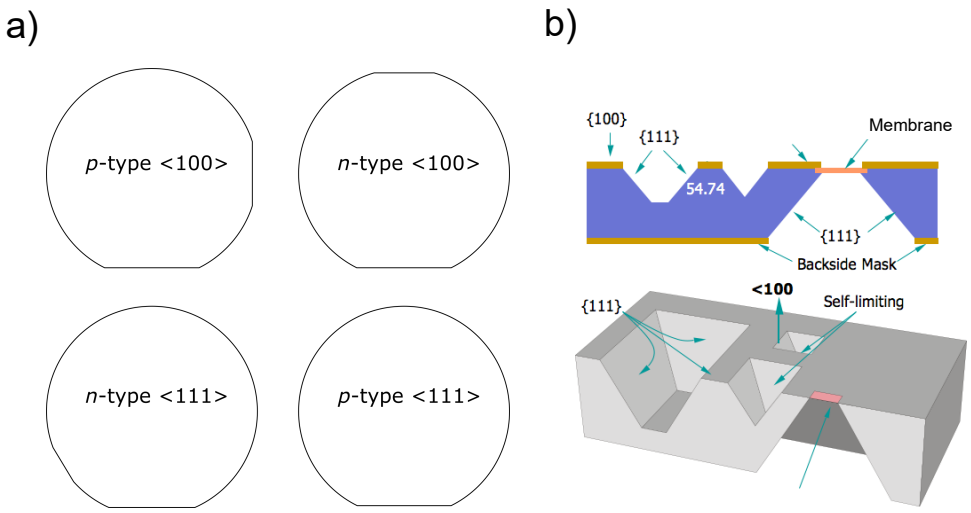

Figure 3–5: Silicon wafer orientation and KOH etching schematic. a) shows an illustration of silicon wafer orientation. The flat usually indicates the doping type and orientation. It may vary depending on substrate supplier. b) shows schematic of KOH etching. 111 plane is a stop plane for KOH etching. KOH etching can produce a invert pyramid shape cavity in 100 silicon wafer.

The specific orientation silicon wafer is required in our project. Since we have to conduct anodic bonding and release silicon nitride membrane by KOH etching, we chose p-type$< 100 >$ silicon wafer which is illustrated in Figure.3–6 (a). $< 111 >$ plane of silicon wafer can prohibit the KOH etching process further. The angle

[1] http://www.lelandstanfordjunior.com/KOH.html

between the norm vectors of $< 111 >$ and $< 100 >$ plane is 54.7°. Thus, the thickness of silicon substrate needs to be considered when design the KOH opening.

After the patterning of the silicon nitride mask on the top, we use 80°C 30% by weight KOH solution to etch $\sim 350\mu m$ silicon. The devices are delicate during the last phase of releasing. Careful manipulation is essential to optimize the yield. The top and back side photo of a device after releasing is shown below:

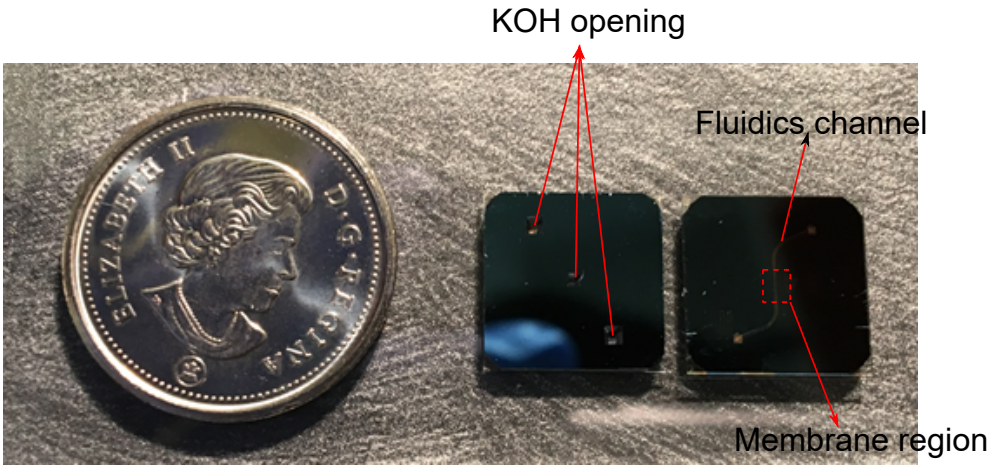

Figure 3–6: Final device compared with the 10 cents Canadian coin. Both front side (left) and bottom side (right) of the device are shown here.

The yield from KOH etching in this process needs to be further improved. We have a relatively low yield on the batch of devices we made for this thesis. More sophisticated membrane releasing strategy is required for future fabrication.

CHAPTER 4
Experiment setup

The experiment setup consists of buffer/samples, microscope and pneumatic regulation system. DNA samples are prepared in Tris-EDTA(TE) buffer and stained with either YOYO-1 or YOYO-3. The pneumatic regulation system is composed of rough manual control valve and fine digital control valve. The digital pneumatic system is controlled by a homemade National Instrument(NI) interface. For microscope setup, we use Nikon Ti microscope to perform fluorescence microscopy. Further, a principle of implement fast switching multi-channels fluorescence microscopy is shown in the same chapter.

4.1 Chemical buffer

We use TE buffer for DNA storage and Tris buffer in experiment. TE buffer is the standard buffer for DNA suspension. Tris, or tris(hydroxymethyl)aminomethane, functions as a pH buffer components. It can stabilize the pH of buffer around 7.1-9.1 which is ideal for nucleic acid. EDTA, or Ethylenediaminetetraacetic acid, is used to scavenge metal ions. Ion depletion can disable the function of metal-dependent enzymes, thus to slow the degradation of DNA. In real experiment, the salt composition and concentration can affect the conformation of DNA and fluorescence intensity[40]. To prevent bias in experiment, we use TE buffer for staining and Tris buffer for experiment.

Both buffers are made in our lab with standard recipe. We prepare 1M Tris buffer as our stock buffer then make small aliquots to avoid contamination. The **1M Tris buffer** is made by the following protocol:

1. Weight 121.1g Tris base with analytical balance.
2. Dissolve Tris base powder with 700ml deionized(DI) water. Stirring is required in this step.
3. Adjust the pH of buffer to 7.5 with concentrated HCl[1] . Appropriate pH probe is required since the pH measurement around 7.0 can be inaccurate with improper instrument.
4. Add DI water and finalize the buffer volume to 1L. Filter and transfer the buffer into a glass container.
5. Autoclave to sterilize. Be aware that a sealing bottle can explode during sterilization.

The Tris-buffer is stocked in a sealed beaker after sterilization. To prepare **1X Tris buffer**, we need to dilute the stock solution 1:100 with DI water. For example, to obtain 1L 1X tris-buffer, we need to mix 10ml stock buffer with 990ml DI water.

To make TE buffer, we need to prepare EDTA solution and Tris buffer first. The recipe to prepare **0.5M EDTA solution** is shown here:

1. Weight 18.6g EDTA with analytical balance.
2. Dissolve EDTA powder in 100ml DI water.

[1] Conduct the adjustment in fume hood to avoid HCl vapor burning.

3. Adjust the solution pH to 8.0 with NaOH. Note that EDTA will not dissolve until the pH reaches 8.0. It will take few hours to dissolve. Stirring is required to mix the EDTA.
4. Filter and autoclave the solution to sterilize. Be aware that a sealing bottle can explode during sterilization.

The TE buffer is also called T10E1 buffer. It has 10mM tris and 1mM EDTA concentration. For example, if we want to get 1L TE buffer, we need 10mL 1M stock tris buffer and 2mL 0.5M EDTA stock solution. Mix the solution together and add DI water to get 1L solution.

4.2 DNA sample

The DNA sample is stored and suspended with TE buffer. We use λDNA and pCMV-Cluc 2 Control plasmid in our experiment. The stock concentration for both kinds of DNA sample are $500\mu g/ml$. We stain and dilute the DNA sample in TE buffer. The stained DNA samples are preserved in fridge at 4°C.

We use YOYO-1 and YOYO-3 fluorophores in our experiment. The staining protocol for these fluorophores are kept the same. The desirable ratio fluorophores molecular to basepairs is 1/8. 2%(by volume) BME is added right before the experiment to minimize the photobleaching effect. The protocol for DNA sample preparation is shown below:

1. Dilute fluorophore(YOYO-1 or YOYO-3)
    - Defrost and centrifuge the fluorophore. The fluorophore should not be thawed frequently.

- Add $2\mu l$ fluorophore to $18\mu l$ 1X TE buffer. Tap the tube to mix. Centrifuge the mixture to gather all solution to the bottom.

2. Dilute DNA sample
   - Withdraw $20\mu l$ DNA sample from the stock. Add $180\mu l$ 1X TE buffer into sample tube. Tap the tube gently.
   - If the sample is λDNA, heat the diluted DNA sample to 60°C then cool it down quickly to prevent fast rearranging.
3. Staining
   - Get a 1.5ml-2ml tube and cover the entire tube with alumina foil.
   - Add $785\mu l$ 1X TE buffer, $15\mu l$ fluorophore and $200\mu l$ diluted DNA sample into the tube. Tap the tube gently.
   - Store the sample in fridge at 4°C. Wait several hrs(for YOYO-1) or 48hrs(for YOYO-3) for mixing.
   - Check the staining result with microscope.

The stained DNA sample here is used as a temporary stock for experiment. It is not ideal to store stained DNA sample for more than 6 months. The temporary stock has DNA concentration $10\mu g/ml$. Before each experiment, we dilute the sample with 1X tris buffer to $1-3\mu g/ml$ depending on the device loading channel geometry. 2%(by volume) BME is added to protect fluorophore from fast photobleaching. We make at least one DNA test slide for each experiment to make sure the staining works properly.

4.3 Pneumatic regulation system

For sample loading and actuating silicon nitride membrane, we have two different pressure controller. The nitrogen pressure is roughly controlled by a manual gas valve on the tank. The outlet of the valve goes into a fine pressure regulator and the lure of loading reservoir. The DNA solution is pushed to the center of device, where is right below the free standing membrane. The membrane is actuated by the fine pressure regulator.

We actuate the membrane via Parker VSO-BT Electronic Benchtop pressure controller running with a custom NI LabVIEW program. The controller is calibrated before each experiment using a manometer.

The digital pressure controller is controlled by 0-5VDC analog input. The output is 0-5VDC which can indicate the real time outlet pressure. Both the input and output signal are connected with a NI DAQ board. The digital pressure controller has a linear response to the input voltage signal. Thus, the calibration is to do a linear fitting for a set of (voltage,pressure) points.The software is programmed with a textbook states machine architecture. The DAQ board can sequentially output a ramping signal so that we can ramp up the pressure within a desired time interval. In this way, the ramping rate can be tuned such that the capture probability reaches its maximum. The inlet gas pressure for the regulator is 50psi. We figured out 15psi is usually sufficient to deflect the membrane to the bottom. To test the depression, we fill our chip with fluorescence solution and vary the pressure. The fluorescence data is shown in the following section:

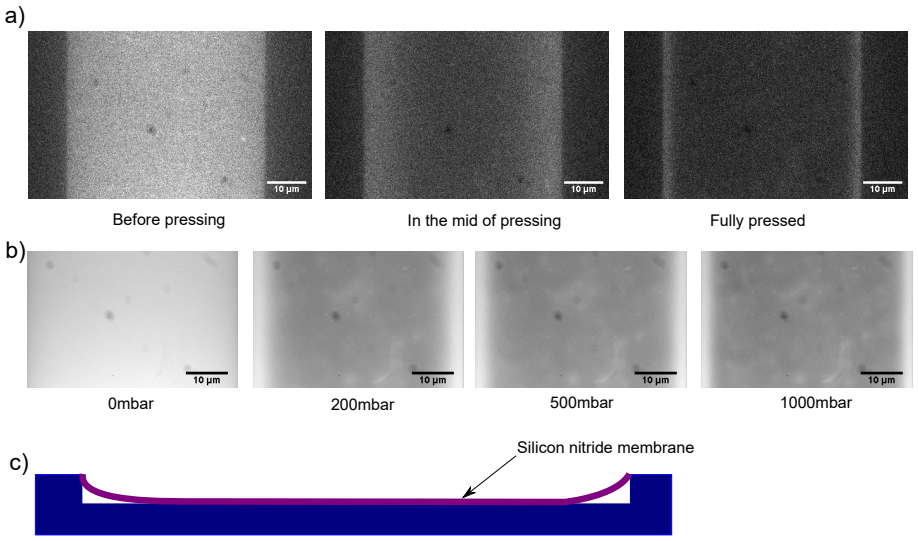

Figure 4–1: Membrane pressing in time and pressure space. a)Membrane is being pressed pneumatically. From left to right, figure shows the pressing before starting, in the middle of pressing and the membrane is fully pressed. Pressure we use here is 1000mbar(14.5psi). b)Membrane is depressed with different pneumatic pressure. The exact pressure we use is marked below the image. c)Schematic graph when the membrane is pressed down. At the channel edge, there will always be space for fluorescence solution, which explains the bright strip at the channel edge in a).

As we can see from the figure, the fluorescent intensity drops dramatically when the pressure is applied. However, we did not see too much changing when apply higher pressure at the center of channel. We do see the strip width getting smaller when we apply higher pressure, which matches our physical intuition. Remarkably, the silicon nitride membrane is flexible enough to survive at least up to 40psi pressure.

Due to the limitation of current pneumatic control system, we can not explore low pressure regime. We are building a ultra low pressure regulation system to provide much precise control over the low pressure regime and hopefully, we will be able to push the membrane with desired height. Our goal is to measure the membrane deflection by correlating the fluorescence intensity with the actual thickness of fluorescence solution.[1]

The loading reservoir is connected with the rough pressure regulator with lure tube. The manual switch can provide us with "on-off" controlling of the pressure, which makes the DNA loading fast and efficient.

4.4 Fluorescence microscopy

We conduct our experiments on Nikon Ti inverted fluorescent microscope. The goal of the microscope is to distinguish the "small details" of the sample we are observing. Typically, we use the word "resolution" to describe the ability of the optical system to distinguish two adjacent point. The resolution of the system is defined by the **diffraction limit** and the **image acquisition setup**.

The diffraction limit is coming from the intrinsic wave property of the light. For microscope, it's the limitation of the objective to distinguish the finest details. This limitation can be calculated from:

$$dx = 0.61\frac{\lambda}{NA} \tag{4.4.1}$$

[1] The space between the silicon nitride membrane and the borofloat glass becomes so small that only a thin layer of fluorescence solution in the middle. In thin film approximation, the intensity of fluorescence is proportional to the film thickness[25].

Where dx is the distance from center to the first dark ring of Airy function. It is the resolution we have for our microscope objective. In our case, we use 100X Nikon Plan Apochromat oil immersion objective with 1.40 numerical aperture. The theoretical resolution of the resolution is $0.2\mu m$. Thus, any details smaller than $200nm$ will be resolved as a Airy disc diffraction pattern. For example, if we observe a $10nm$ diameter fluorescent bead, the image we will get from microscope is much larger then the exact size of bead. The signal can be fitted by a Airy disc function and the distance between the center circle to the middle of the first dark ring will be around $200nm$, which can be confirmed by the calculation above. Further, the DNA image captured by the setup is a convolution of fluorescence molecules distribution function with PSF function.

Beside the diffraction limit, the image acquisition setup can affect the quality of image as well. The acquisition equipment's function is to convert light signal, photon number or light intensity in our case, to electrical signal which is the digitized image in our computer. The most common facility is **charge-coupled device(CCD)** and Boyle and Smith were awarded with Nobel Prize in Physics division at 2009. There are two sources for the aberration. **thermal noise** of the CCD and the **sampling deficiency**. Thermal noise is an intrinsic fluctuation noise source. Cooling the CCD chip can reduces the thermal noise, thus the "dark current". It can improve the sensitivity of the CCD when the light intensity is low. A typical image of a DNA chain on a test glass slide with our setup is shown below:

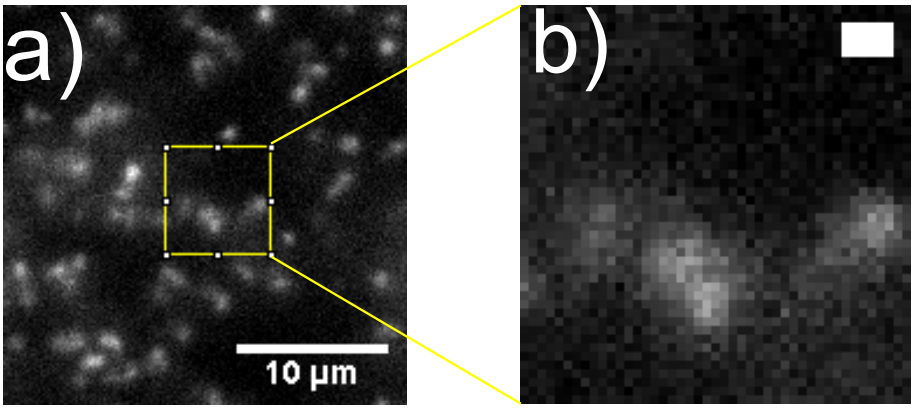

Figure 4–2: Fluorescence microscopy image from YOYO-1 stained λDNA on a test glass slide. a) Sample image with multiple DNA chains in the field of view. b) A zoom in view of the sample slide. The scale bar is $1\mu m$

X-Cite 120Q excitation source is used as our broad bandwidth excitation lamp source. The FITC filter and Texas Red filter cube set are provided by Chroma Technology. To minimize the effect of photobleaching in our experiment, we use 25% light intensity for all our experiments. The intensity is adjusted by the internal iris of X-Cite lamp. Andor iXon+ EMCCD is coupled to our microscope. In Fig. 4–4(b), the background signal fluctuation is observed. The signal level keeps changing slightly at the region without DNA chain. This time-dependent fluctuation can be suppressed by cooling the CCD chip. The cooling system embedded in Andor iXon+ can cool the chip down to -70°C. Theoretically, EMCCD can have the minimum dark current when the temperature is down to around 170K. The periphery cooling system is needed to optimize the performance.

Beyond the thermal noise, sampling deficiency sometimes can be a problem for microscope setup. **Nyquist-Shannon sampling theorem** tells us[1] :

"*If a function $x(t)$ contains no frequencies higher than B hertz, it is completely determined by giving its ordinates at a series of points spaced 1/(2B) seconds apart.*"

The finest resolution is defined by diffraction limit which is about $400nm$ with our objective. The CCD chip should at least distinguish two points $200nm$ away. After the amplification of objective, $200nm$ in the image plane becomes $20\mu m$ when the light reach the CCD chip. Our CCD camera has $16\mu m \times 16\mu m$ square pixels. The separation is slightly smaller than the need from diffraction limit. Thus our experimental data is captured properly without information distortion.

After clarifying the microscope we are using, I will briefly introduce the way we capture 2 colors data in this experiment. The turret mounted on our microscope has the ability to rotate mechanically and it can be controlled through Nikon Element software. The capture sequence can be illustrated as follow:

[1] From https://en.wikipedia.org/wiki/Nyquist-Shannon_sampling_theorem

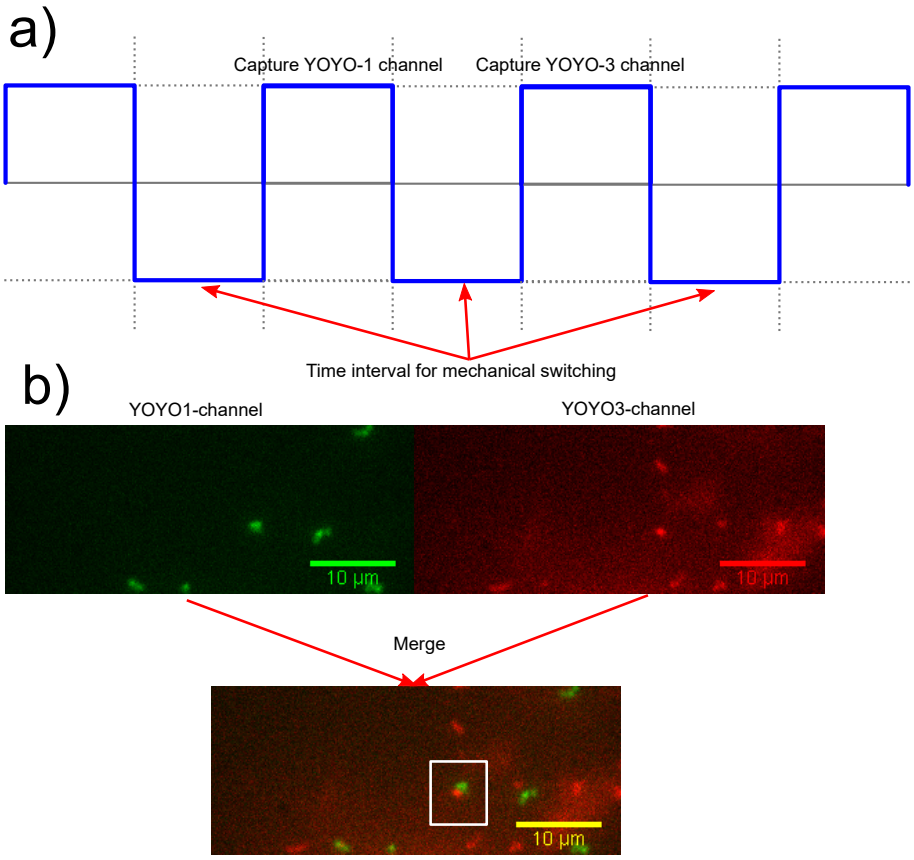

Figure 4–3: Procedure of capturing two channels images by mechanical turret. The schematic square does not reflect the real condition in experiment. a)The system will capture the first image in YOYO-1 channel, then the turret will switch from FITC cube set to Texas Red cube set. The second image will be captured with YOYO-3 is excited. After capture the turret will switch back to FITC cube set.b) A typical fluorescence image without image enhancement. YOYO-1 channel and YOYO-3 channel data are overlaid and a two DNA chains trapping event appears in the cavity labeled by white rectangular.

The two colors images are composed by superposition of two channel data from each period. The system is synchronized by the inner-clock of computer. The mechanical rotation of filter turret takes time. The frame rates we reached after leverage the exposure time for signal quality is 0.84 fps, or a single molecule our of the pair can be imaged in a single channel at 23.49fps.

The simple mechanical turrets can help resolve the two-chain interaction problem roughly. The **Nyquist-Shannon sampling theorem** generates problem. If we want to resolve the time-dependent dynamics parameter accurately, we have to capture at least twice faster than the dynamics pattern. This time is defined by the decorrelation time which I will discuss later. It is roughly $2s$ in two-chains observation. Thus, the minimum frame rates should be 1fps. Besides the deficiency of frame rates, we have a long time interval(around 600ms) between two channels, but we assumed the two channel images are taken simultaneously. This systematic bias can appear along with the entire experiment.

4.5 Fast switch LED system in fluorescence microscopy

By the time I write this thesis, we have developed a color switchable LED lamp system to overcome the time resolution problem of our setup. The channel switching speed is improved substantially and the speed limitation now is set by the frame transfer speed of the EMCCD.

Unlike the mechanical switch filter turrets, we switch the excitation light source instead of the filter cube. An illustration of the setup is shown below:

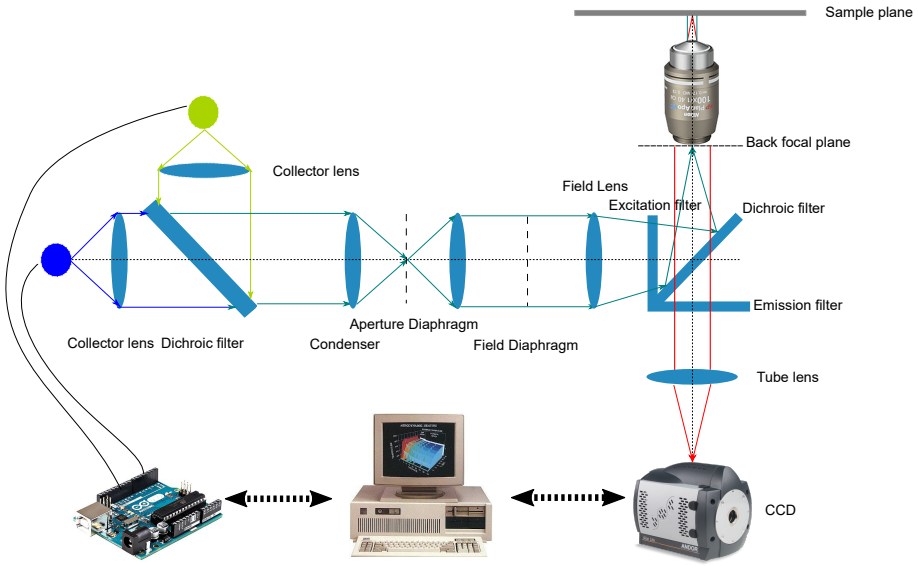

Figure 4–4: Schematic of the fast switching microscope system. The blue and green circles represent LED chips. The classical Kohler illumination system is inherited from the Nikon Eclipse Ti microscope. The first dichroic mirror merges two LED source into once beam. The second dichroic mirror has two distinct bandpass.

The second dichroic filter is embedded in the filter cube. It has two bandpass which allows both YOYO-1 and YOYO-3 work properly. With the blue LED(470nm) working, the YOYO-1 fluorophore is activated and vice versa. Thus, the filter cube can safely stay in path. The working time of the LED light is controlled by TTL signal through arduino board. The setup building is inspired by Bosses' work[6]. The new setup has been characterized and the a summary is shown below in Figure.4–6:

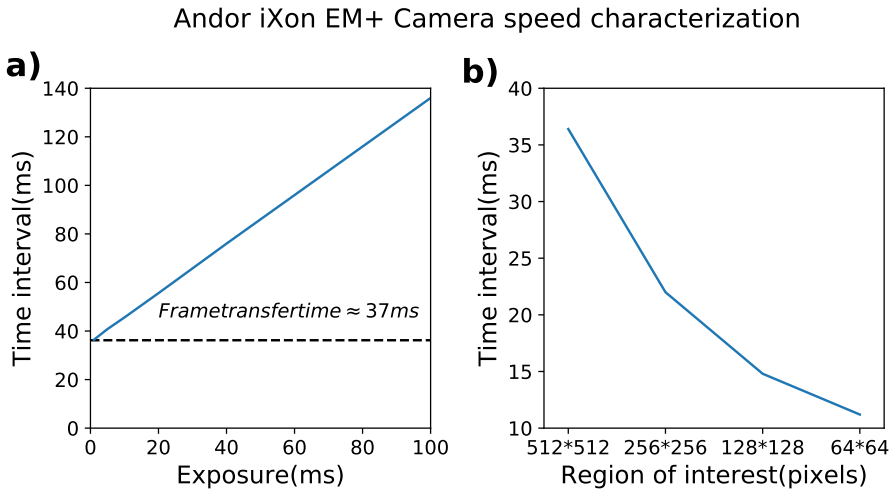

Figure 4–5: Capture speed characterization of dual-LED setup. Time interval shown in the graph is the time difference between adjacent frames when using single channel capture. For two channel capture, the time interval should be doubled. a) The time interval for difference exposure time. The bias when exposure equal to 0 is the frame transfer time for CCD chip. The measurement is performed on a $512 * 512$ region. b) The time interval for different size of region of interest when exposure time is fixed at $1ms$. The frame transfer time decreased substantially by reducing the pixel numbers on the chip.

Both color LED chips are supplied by Luxeonstar[1] and the power modules has the capability to switch between on/off status within $5\mu s$. The short switching time is ideal in our application since the fire trigger is overlaid with the exposure. The intensity of both lines can be adjusted manually. To make the data consistent, we use the max LED intensity and neutral density 8(ND8) filter in imaging. The sample image for YOYO-1 channel and YOYO-3 channel with LED source is shown below:

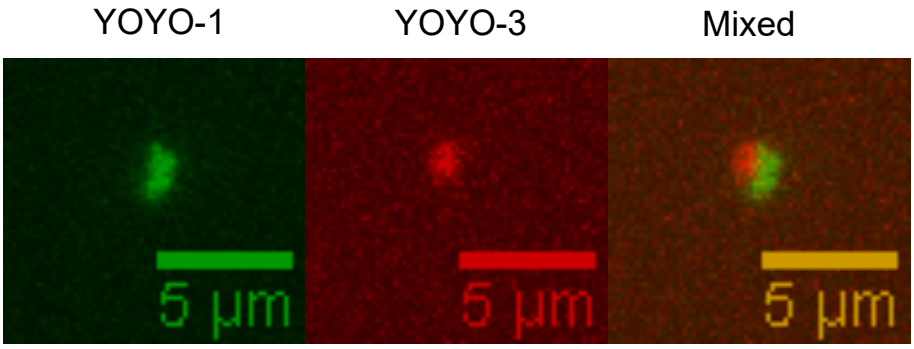

Figure 4–6: Experiment sample data by dual-LED setup. We use $20ms$ exposure time to minimize the time delay between two channels. 300 EM-gain is applied to increase the signal-noise ratio. The region of interest is also cropped down close to the edge of nanocavity to minimize the frametransfer time.

We connect the fire trigger TTL line of CCD to the digital input of Arduino uno board. The TTL signal is at hight voltage level when the camera is in exposure and low level when it is in frame transfer model. The board is programmed by

[1] https://www.luxeonstar.com/

MicroManager[2] that it can work through a user-friendly interface. The captured data will be saved temporally in CCD camera and the different channels will be distinguished and labeled by MicroManager after the date being transferred to PC.

[2] https://micro-manager.org/wiki/Arduino

CHAPTER 5
Data analysis

We use the mechanical turret setup to capture all the data presented in the section. I and my lab mate Xavier Capaldi have coauthored on a paper[8] presenting the device and the DNA chain conformation and dynamics measurement under cavity confinement. As the first application on this device, we confined single and two differentially stained DNA chains inside a $2\mu m \times 2\mu m$ square cavity. We studied the *single* and *double* polymer chains conformation and dynamics under this cavity confinement.

The fundamental physics problem involved in the cavity confinement system is, how does polymer chain behave in quasi 0D confinement when the second chain presents. The studies in quasi-2D(slit-like confinement) and quasi-1D(nanochannel confinement) are relatively completed compared with quasi-0D(nanocavity confinement). The conventional static fused-silica thermal bonded device lessees the ability to confinement polymer chain into cavity. We solve this problem by coupling the flexible membrane lid which can be actuated pneumatically with cavity. The cavity is $200nm$ in depth which is less than half of the radius of gyration of λDNA in bulk

solution($\approx 0.7\mu m$). The width of the cavity is $2\mu m$. The radius of gyration projection in $x-y$ plane could[1] be larger than it is in bulk regime. For single chain, the lateral confinement is qualitatively classified in weakly confinement regime. For two chains trapped in a cavity, the lateral confinement transits dynamically in an altered regime. The chain-chain interaction influences the chain conformation and dynamics considerably. Further, we explored the affect of different topology chain in multiple chain interaction with circular shape plasmid DNA substrate. The system can be developed in a way that mimics biological system, such as E.coli and DNA stored inside a compact nucleus, which might give some insights on complex bio-process.

5.1 Data format and the pre-process

The DNA chain substrates are λDNA stained with either YOYO-1 or YOYO-3, and pCMV-Cluc 2 Control Plasmid DNA stained with YOYO-3. The device is mounted on a home designed 3D printed chuck which matches the move stage of our microscope. Background intensity are calibrated before we load DNA sample. The background intensity is averaged over 100 frames.

For each DNA sample, we captured 10-15 videos containing 100 frames. We cropped the regions down to the cavities where DNA chains are confined. We subtract the background intensity to reduce the background noise. A time-series of single-molecule and two-molecule dynamics in a cavity is shown below:

[1] As we reviewed in Chap2, it is still a debating problem for the transition from weakly confined regime to de Gennes regime.

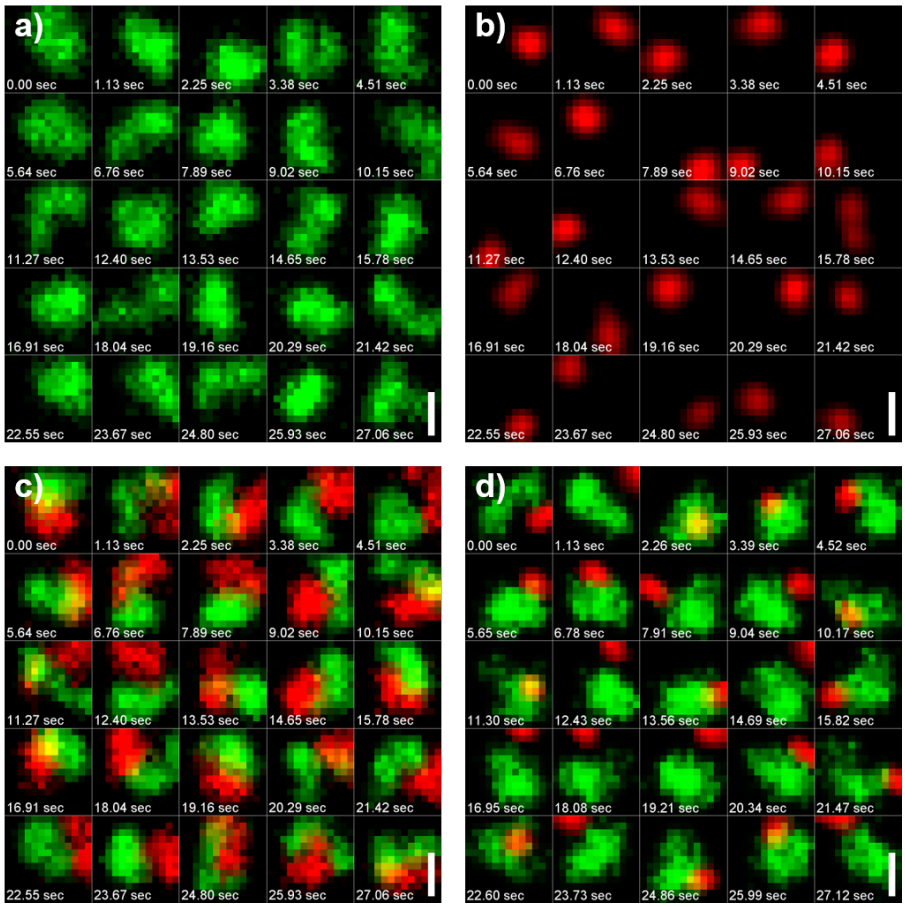

Figure 5–1: Fluorescence videomicroscopy frames of cavity confined DNA for cavities with lateral dimension of $2 \times 2\,\mu\text{m}^2$. (a) Single λ-DNA trapped in a cavity. (b) Single plasmid trapped in a cavity (c) Two differentially stained λ-DNA molecules in a nanocavity. (d) A λ-DNA (green) and plasmid molecule (red) confined in a cavity. The green color indicates DNA stained with YOYO-1 while the red color indicates DNA stained with YOYO-3. Scale bar is $1\,\mu$m.

We picked two distinct cavities to valid our date from the fabrication defect influence. The physical behaviour in each cavity is observed to be identical. Comparing

Fig. **??**(a) and (c), the DNA chain is confined more with the second chain present qualitatively. In the case of single molecule confinement(λDNA), the molecule prefers to remain in the cavity center. In the case of two molecules confinement(λDNA-λDNA), two molecules segregate and the center of the molecule coils are displaced from the cavity center. The two molecules appear to undergo a Brownian 'rotation' about the cavity center. However, the plasmid and λDNA does not show apparent segregation effect. Interestingly, some frames indicate the plasmid and λDNA overlapping(Fig. **??**(d)).

5.1.1 DNA position analysis

To quantify the observations above, we conduct image analysis to track the fluorescence center-positions of the cavity confined molecules. The center-position of λ-DNA is calculated by a weighted average of position coordinates over the single-molecule fluorescence distribution in the cavity:[5]

$$\mathbf{r}_{CM}(t) = \frac{\int \mathbf{r} \cdot I(\mathbf{r}, t)\, \mathrm{d}^2\mathbf{r}}{\int I(\mathbf{r}, t)\, \mathrm{d}^2\mathbf{r}}. \tag{5.1.1}$$

The quantity $\mathbf{r}(t)$ is the position vector; the integral is performed over a ROI that corresponds to the cavity. $I(\mathbf{r}, t)$ represents the intensity at position $\mathbf{r}$. To reduce the influence of time-dependent background fluctuations on the position detection, we apply a Gaussian filter to the image prior to using Eq. 5.1.1. The plasmid, due to its circular supercoiled topology and smaller size,[20, 34] has a more compact fluorescence distribution that corresponds to a diffraction-limited Airy disk spot. Plasmid's Airy spot can be sufficiently tracked with the ImageJ Mosaic Particle Tracking plugin. The tracking result is shown below:

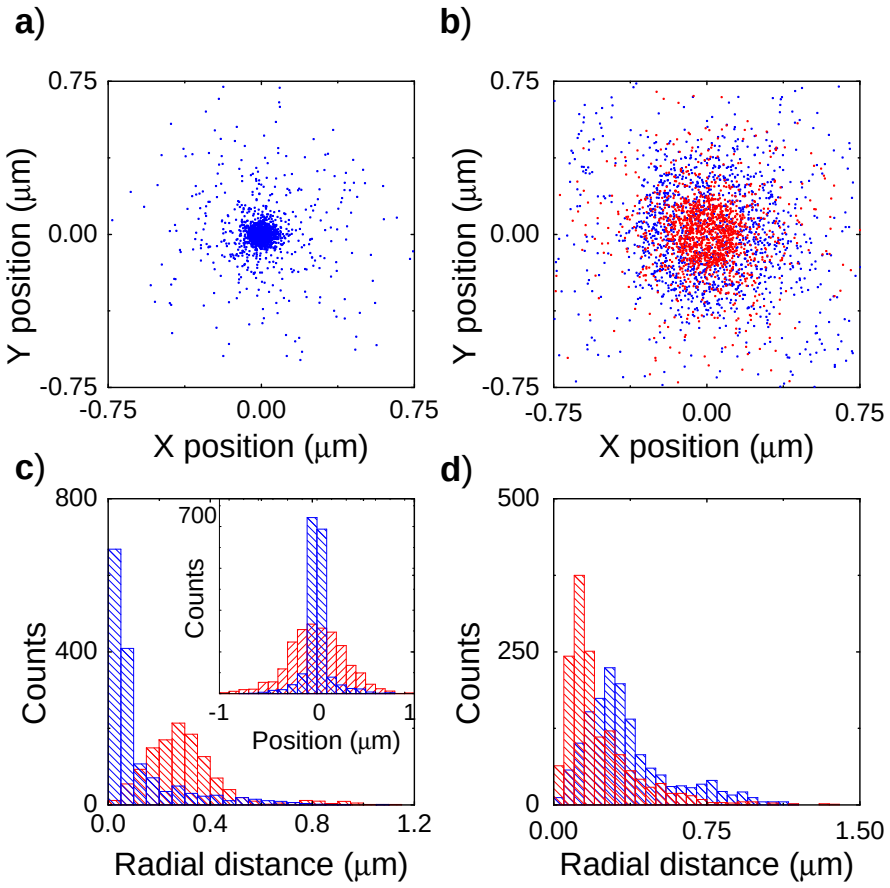

Figure 5–2: Center position analysis for λ-DNA. (a) Position distribution for a single λ-DNA trapped in the cavity. (b) Position distribution for two λ-DNA molecules in the cavity. Blue squares indicate YOYO-1 stained chain; red squares indicate YOYO-3 stained chain. (c) Radial distance histogram of λ-DNA chain. Blue shaded columns indicate distribution of single λ-DNA trapped in cavity. Red shaded columns indicate distribution of λ-DNA in cavity while the second λ-DNA is present. The inset shows for the same quantities the horizontal projection of the distribution along the cavity width. (d) Histogram of radial distance for λ-DNA in presence of second λ-DNA. Red shaded columns indicate YOYO-3 stained chains; blue shaded columns indicate YOYO-1 stained chain.

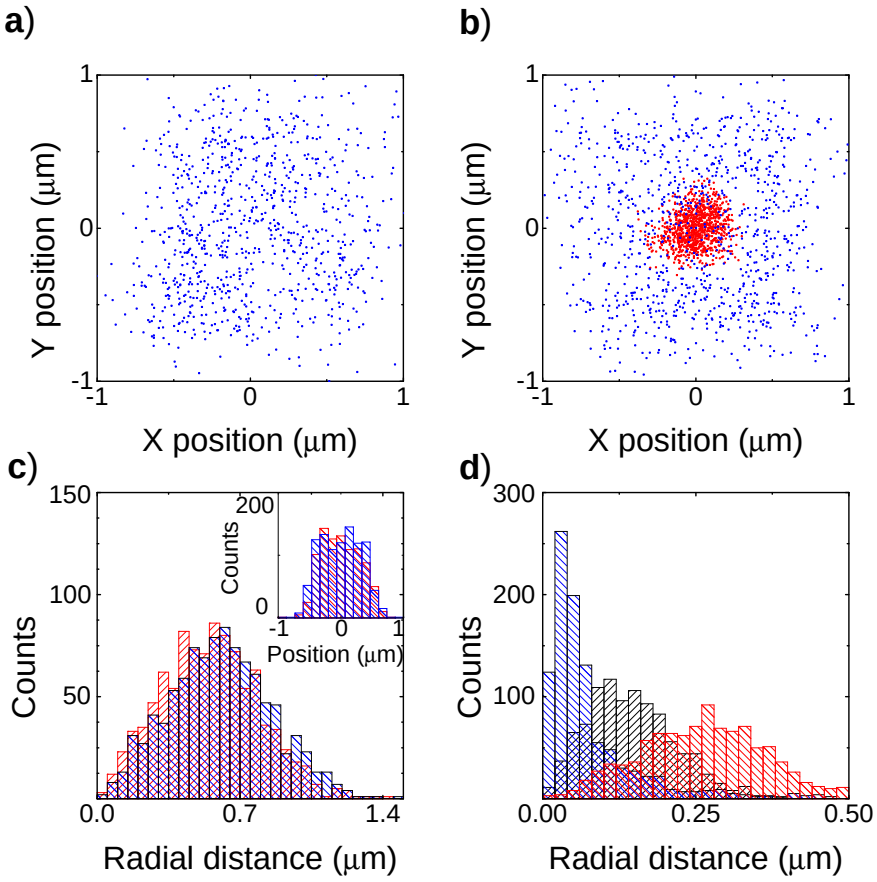

Figure 5–3: Center position analysis for plasmid DNA. (a) Position distribution for a single plasmid trapped in the cavity. (b) Position distribution for a plasmid trapped with λ-DNA in the cavity. Blue squares show plasmid positions; red squares show λ-DNA positions. (c) Radial position distribution of plasmid. The blue shaded columns show the distribution for single plasmid; red columns show the plasmid distribution when a λ-DNA is also present. The inset shows for the same quantities the horizontal projection of the distribution along the cavity width. (d) Histogram of radial distance of λ-DNA. The blue shaded columns indicate the distance distribution for single λ-DNA trapping. Black shaded columns indicate the distribution of λ when the plasmid is also present. The red shaded columns indicate the distribution when two λ-DNA molecules are trapped.

Figure 5–2(a) shows the fluorescence center-positions distribution for a single λDNA molecule trapped in a cavity. As the radius of gyration projection of λDNA under $200nm$ z-axial confinement is comparable with and cavity dimensions, chain-wall interactions are quite strong and the λDNA is excluded from the cavity corners and periphery. The exclusion leads to the center-position distribution tightly localized in the cavity middle. Figure 5–3(a) shows the position distribution for a single plasmid. As the plasmid has a much smaller gyration radius than the λDNA, the chain-wall exclusion effect is weaker, thus plasmid can explore a greater portion of the cavity. In fact, we observe that the distribution is spatially uniform and follows the square cavity shape.

Figure 5–2(b) shows the position distribution of two λDNA molecules. When the second chain is present, due to excluded volume interactions between the coils, the center-position of the chains are forced to explore a greater portion of the cavity, creating a broader position distribution (see Fig. 5–2(c)). In addition, we find that the center position distribution for the YOYO-3 labeled chain is slightly more concentrated in the cavity center than the distribution for the YOYO-1 labeled chain (see Fig. 5–2(d)). This effect might arise from how the different stains alter the chain contour, stiffness and self-interactions. YOYO-1, for example, increases the contour length of DNA[29] and there are likely differences in intercalated length between the two stains. A molecule confined in a cavity will have its coil sized fixed by the cavity confinement, but a longer contour length will decrease the chain's entropic elasticity. Possibly, when the stains alter the contour length differentially, the slightly longer and more easily deformed chain is pushed to the cavity periphery as the chain closer

to the periphery is required to deform more to adopt a greater circumferential extent and conform to the square cavity geometry.

Figure 5–3(b) shows the position distribution of λ-DNA and the plasmid when they are trapped together. We observe that the position distribution of the plasmid DNA is not altered by the presence of λ-DNA (Figure 5–3(c)), but that the position distribution of λ-DNA is less concentrated in the cavity center (Figure 5–3(d)). The plasmid, with its supercoiled circular topology, will have a compact anistropic structure and act–very crudely speaking–like an elongated pancake.[20, 34] This structure, once aligned with the cavity surfaces, might penetrate the λ-DNA structure relatively easily by passing through the depletion region of lowered DNA concentration near the cavity walls.[42] This effect, which is consistent with Fig. 5–1(d), would then explain why the 2D plasmid position distribution is not altered by the λ-DNA. We argue that the shifting of the λ-DNA position distribution might be explained by a depletion interaction induced by the plasmid [16]; by getting closer to the cavity edges, the λ-DNA frees up more volume for the plasmid conferring greater translational entropy.

5.2 DNA diffusion analysis for single chain trapping

The dynamics of DNA molecule can be measured by tracking the fluorescence center of mass. The single chain diffusion in a cavity follows the anomalous diffusion pattern and can be modeled as the free Brownian diffusion of a particle within an infinite square well potential.[30] The molecule's mean-square displacement along x given by:

$$MSD(\delta t) = \frac{1}{T}\int_0^T [x(t+\delta t) - x(t)]^2\, dt \tag{5.2.1}$$

Since our device is symmetric in the x and y directions, with the coordinate system aligned with the cavity dimensions, the mean square displacement is the same along the x and y axis and we average results obtained for x and y. The mean-square displacement can be obtained by solving the diffusion equation for a particle in a square box, leading to:

$$MSD(\delta t) = \frac{L^2}{6} - \frac{16L^2}{\pi^4} \sum_{n=1,3,5\cdots}^{\infty} \frac{1}{n^4} \exp\left[-D\left(\frac{n\pi}{L}\right)^2 \delta t\right] \tag{5.2.2}$$

where L is the box width.[30] As the molecules have a finite size, a zone of excluded-volume will exist about the cavity boundary and the L values extracted will be smaller than the true lateral cavity dimensions. We show the experimental MSD with theoretical fit according to Eq. 5.2.2 in Fig. 5–4. Both the diffusion constant D and box width L are fitted.

The DNA diffusion constants obtained are $D_\lambda = 0.055 \pm 0.003\,\mu\text{m}^2/\text{s}$ (for λ-DNA) and $D_\text{p} = 0.68 \pm 0.02\,\mu\text{m}^2/\text{s}$ (for plasmid). In bulk, $D_{\text{bulk},\lambda} = 0.47 \pm 0.03\,\mu\text{m}^2/\text{s}$ [44] and in a 200 nm nanoslit $D_{\text{slit},\lambda} = 0.1\,\mu m^2/\text{s}$[47, 2], so that cavity confinement creates a two-fold reduction with respect to the slit and a factor of ten with respect to bulk. For a 6.5 kpb plasmid the bulk diffusion constant $D_{\text{bulk, p}} = 2.89\,\mu\text{m}^2/\text{s}$;[54] cavity confinement thus leads to a 4-fold reduction with respect to bulk. The extracted confinement dimension L of λ-DNA is $0.13 \pm 0.002\,\mu\text{m}$ while the confinement dimension of the plasmid is $1.57 \pm 0.01\,\mu\text{m}$. The radius of gyration for λ-DNA confined in a 200 nm slit is: $r_{g,\lambda} = 0.91\,\mu\text{m}$.[32]. Using $2r_g$ as an estimate of the molecule coil extent, we estimate that the confinement dimension $L \approx d - 2r_g$ where $d = 2\,\mu\text{m}$ is the cavity width. The resulting small value $L_\lambda \approx 0.2\,\mu\text{m}$ is quite comparable to

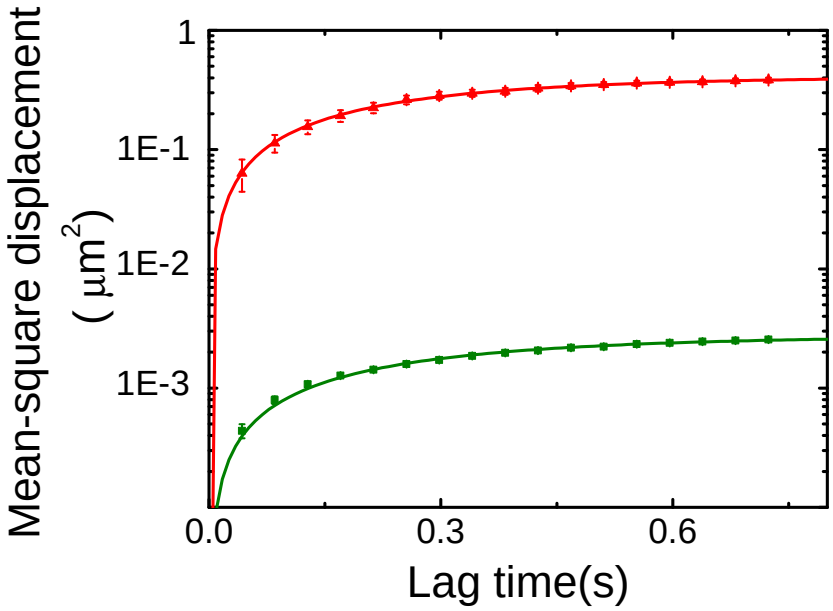

Figure 5–4: Mean-square displacement for single λ-DNA trapping (green triangles) and single plasmid trapping (red squares). The solid curve is the fitted diffusion model.

our measurement, reflecting a scenario where the molecule's center-of-mass position is tightly confined (i.e. the molecule has very little room to move before bumping into a cavity side-wall). To estimate the spatial extent of the plasmid, we use measurements for the ColE$_1$ plasmid, which is of comparable size (6.65 kbp). Voordouw *et al.*[54] report that for ColE$_1$ light scattering measurments give $r_g^{\mathrm{p}} = 104\,\mathrm{nm}$, so that $L_{\mathrm{p}} \approx 1.79\,\mu\mathrm{m}$. This is the right magnitude but larger than then the L_{p} value we measure, a difference which might arise from plasmid anisotropy and our lower ionic strength.

5.2.1 Position auto-correlation calculation

We investigate the position auto-correlation of the λ-DNA and plasmid molecule for both single molecule and two-molecule trapping (see Fig. 5–5). The position auto-correlation function is defined as:

$$C_{auto}(\delta t) = \langle x(t+\delta t)\, x(t) \rangle_t \tag{5.2.3}$$

where x represents position along either the $x-$ or $y-$ direction with the origin located at the cavity center. The angle bracket indicates a time-average, corresponding to averaging over the entire video length; δt is the correlation lag time. Considering the square symmetry of the cavity, we average the position auto-correlations for the $x-$ and $y-$ directions.

Figure 5–5(a,b) shows the autocorrelation functions for single and two-particle trapping; these are well-descibed by a single exponential function. We define the decorrelation time as the time needed for the correlation function to decay to e^{-1} of its maximum value. The decorrelation time for λ-DNA trapped in a cavity, if no other molecules are present, is 0.25 ± 0.01 s; the decorrelation time for λ-DNA, trapped in the presence of a plasmid, is 0.29 ± 0.01 s and the decorrelation time for λ DNA trapped in the presence of a second λ-DNA molecule is 2.00 ± 0.1 s. The decorrelation time clearly increases with the presence of additional molecules, and in the case of λ-DNA increases by almost an order of magnitude. The decorrelation time for a plasmid, if no other molecule is trapped, is 0.31 ± 0.01 s; in the presence of a λ-DNA molecule the decorrelation time is 0.39 ± 0.01 s. Qualitatively, we believe that the increasing decorrelation times for two-molecule trapping arise as the second

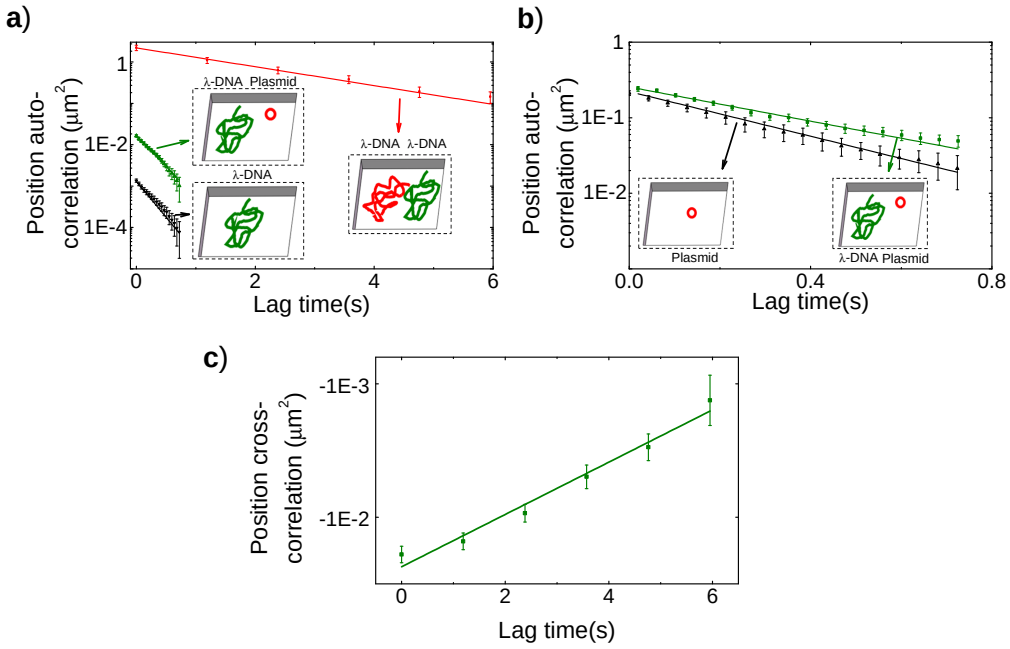

Figure 5–5: Position auto-correlation as a function of lag time on a log-linear scale with an exponential fit. (a) Position auto-correlation function for λ-DNA. Red squares indicate the correlation function measured for a λ-DNA molecule trapped in a cavity when there is a second λ-DNA molecule trapped in the same cavity. Green upper triangles indicate the correlation function obtained for λ-DNA when there is a plasmid molecule also trapped in the cavity with the λ-DNA. Black lower triangles indicate the correlation function measured for a λ-DNA molecule trapped in a cavity when there are no other molecules present. (b) Auto-correlation function for plasmid DNA. Green squares indicate the position correlation function of the plasmid in the presence of a λ-DNA molecule trapped in the same cavity as the plasmid. Black upper triangles indicate the position autocorrelation function for the plasmid with no other molecules present. (c) Position cross correlation for trapping of a YOYO-1 stained λ-DNA and a YOYO-3 stained λ-DNA. Exponential fits are shown as bold curves in the same color as the data points. Error bars correspond to standard error arising from measurements over an ensemble of 10 different molecules undergoing equivalent dynamics.

molecule transiently confines the first molecule creating a caging effect. Caging leads to a lower effective diffusion constant for the molecules that then increases the overall decorrelation time.

We also investigate the position cross-correlation between the YOYO-1 stained λ-DNA chain and the YOYO-3 stained λ-DNA chain (Figure 5–5 (c)). The cross-correlation is defined as

$$C_{cross}\left(\delta t\right) = \left\langle x_{\text{yoyo-1}}\left(t+\delta t\right) x_{\text{yoyo-3}}\left(t\right)\right\rangle_t \tag{5.2.4}$$

where $x_{\text{yoyo-1}}$ and $x_{\text{yoyo-3}}$ represent respectively the position of the YOYO-1 stained chain and the YOYO-3 stained chain at time t along the $x-$ or $y-$ direction. Again, we average the cross-correlation function over x and y directions. The cross-correlation function is negative, indicating anti-correlation arising from the strong segregation between the molecules. The decorrelation time of the cross-correlation is $2.8 \pm 0.3\,\text{s}$, comparable in order of magnitude to the autocorrelation decay time; we hypothesize it is longer than the autocorrelation decay time as the cross-correlation function decorrelates over the time-scale required for *both* chains to loose their initial joint conformation.

5.2.2 Intensity cross-correlation function

As a final measure of the two-chain dynamics, for the case of two λ-DNA molecules we investigate the cross-correlation of the intensity across the cavity. In particular, we compute the intensity cross-correlation function $\langle \delta I_{\text{yoyo-1}}(x,y,t)\delta I_{\text{yoyo-3}}(x,y,t+\delta)\rangle$, where δI gives the fluctuation away from the average intensity at position (x,y)

inside the cavity. Figure 5–6(a-c) shows the intensity cross-correlation for three different times. We find that there is a strong anti-correlated annular well for short times, consistent with the organized rotation of the segregated conformations observed in Fig. 5–1c. The 'hill' of slightly reduced anti-correlation in the cavity center corresponds to configurations where the molecules have drifted to the center and partially mixed, leading to a slight breaking of the organized rotational dynamics and a reduction in anti-correlation. We also compute the cross-correlation function averaged over the entire cavity region (Fig. 5–6(d)). The averaged cross-correlation is described well by a single exponential decay and has a decorrelation time of 4.2 ± 0.4 s. This value is comparable in magnitude but slightly larger than the position cross-correlation decay time. We speculate that the position cross-correlation decay time is lower because of the greater confinement of the molecule center positions relative to a particular individual segment or portion of the molecule. The greater confinement of the molecule centers implies that the center positions have to migrate over a smaller distance to swap positions compared with the distance an individual segment needs to traverse to return to a particular location of the cavity.

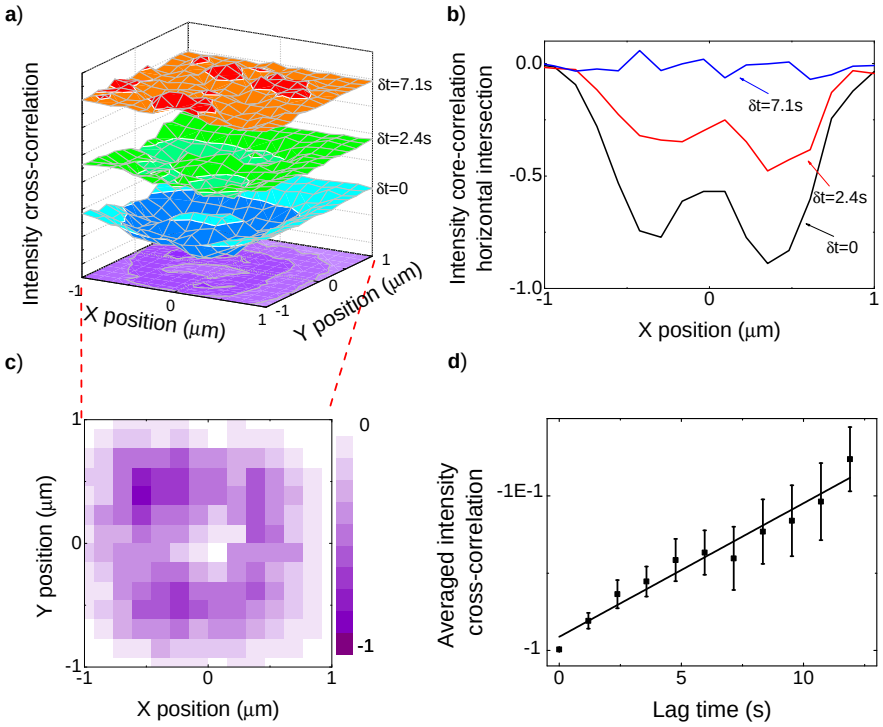

Figure 5–6: Intensity Cross-Correlation Function. (a) Surface plot for normalized intensity cross-correlation for different lag times. Orange surface represents cross-correlation function at $\delta t = 7.1s$, green surface represents cross-correlation function at $\delta t = 2.4s$ and blue surface represents cross-correlation function at $\delta t = 0$. (b) Intensity cross-correlation function from (a) taken along a slice along the x-axis for $y = 0$. (c) Intensity cross-correlation for $\delta t = 0$. (d) Intensity cross-correlation function averaged across cavity verses lag time. The correlation function is fitted with an exponential function that is shown as a black solid curve.

CHAPTER 6
Conclusion

6.1 Conclusion

We have developed a device based on pneumatically actuated flexible membrane lids to capture single and multiple DNA molecules in a cavity. We find that the molecular organization and dynamics is strongly affected by whether more than one molecule is captured. A single λ-DNA molecule has coil extent on the order of the cavity width. When two molecules are confined together, they exist in a highly partitioned state and appear to undergo a Brownian rotation about the cavity center. We find that even the presence of a small plasmid molecule can alter the λ-DNA state, tending to pull it away from the cavity center. Confinement of more than one molecule has additional non-trivial effects on dynamics, tending to increase overall relaxation times for confined molecular diffusion.

Our system and observations raise some intriguing questions. For example, how might the properties of the organized multiple molecule states vary as a function of the molecule size ratio, molecule number and cavity geometry? Might distinct dynamical regimes exist for two, three or multiple molecule states as a function of cavity dimensions and size ratio? How does varying the vertical dimension effect molecule partitioning? (Does chain mixing occur as bulk conditions are approached?) Another potential experiment is to only lower the lid partially, so that escape from our traps is possible upon application of a sufficient driving force to overcome the free

energy differential. Our system would then enable exploration of how the presence of multiple chains affects escape kinetics. In addition, while the cavities used here are not designed to mimic specific biological systems, our approach can be used to construct cavities close in dimension to bacteria and eukaryotic nuclei. Using extracted *E. coli* genomes[39] to model native Mbp scale DNA representative of bacterial genomes and (crudely) chromosomes of lower eukaryotic cells, we can then create experimental models isolating the effects of confinement from other sources of biological complexity.

We can already compare our experimental results on partitioning/mixing to a proposed phase-diagram deduced for self-avoiding chains by S. Jun *et al.*[27] S. Jun *et al.* uses polymer scaling arguments to predict a phase-space for chain segregation/mixing that depends only on polymer concentration and confinement. Polymer concentration is measured by the ratio r_F/ζ, where r_F is the Flory radius and ζ is the chain correlation length; confinement is measured by r_F/D where D is the dimension of imposed confinement. For the λ-DNA, estimating the Flory radius by the chain gyration radius ($0.7\,\mu$m), taking D to be the cavity depth (200 nm) and estimating ζ as the coil extent ($0.91\,\mu$m), we find that $r_F/D = 3.5$ and $r_F/\zeta = 0.77$, which lies in a region of space corresponding to segregation. For the plasmid, following the argument used in S. Jun *et al.*, we take r_F to be 104 nm (plasmid coil size) and let ζ correspond to the correlation length of the much larger molecule (λ-DNA), leading to $r_F/D = 0.52$ and $r_F/ = 0.11$, which lies in the region of the space where mixing is predicted. So, while we do not see evidence of segregation of plasmids and λ-DNA, this is consistent with the theoretical prediction for self-avoiding chains. Possibly

plasmid exclusion requires higher chain concentration, more complex chain topology (e.g. supercoiling[27]) and/or presence of chain condensing agents, like molecular crowders.[28, 10] We plan to explore these effects in future experiments, using extracted *E. Coli* genomes.

Our observation, however, that the presence of a single small compact molecule can impact the behaviour of a larger coil in confinement is unexpected and intriguing. For example, might we detect differences between linearized and circular form plasmids? How does this effect scale with plasmid size and plasmid number? In addition, we show that subtle differences due to chemical stains (e.g. YOYO-1 versus YOYO-3) can be detected via two-molecule measurements of the chain position distributions. Possibly, this effect could extend to other types of molecular labeling or protein-interactions. Overall, our results suggest that measurements of the physical interactions of multiple confined macromolecules might convey information beyond that of a purely single molecule experiment. From a theoretical point of view, Monte Carlo and Brownian dynamics simulations of multiple chain confinement might clarify the underlying mechanisms responsible for these observations.

CHAPTER 7
Latest work in multiple chains system: chain swapping in a cavity

In the previous experiment, we see the two chains system behaves as a "Brownian rotor" under cavity confinement. By the data presented in this section, we observe the configuration changing of two chains system with cavities in different shape. Conformation changing can unveil the transition from "Brownian rotor" phase to "Segregation" phase. This phenomena by it's own right is interesting physically and might shine light on the physical reason of geometry changing of cell in division process[18]. Given cell tends to elongate during anaphase and telophase, the cell elongation actually breaks the spacial symmetry and creates a free energy barrier, which physically makes the segregation configuration more favorable.

In the experiment data presented here, we change the geometry of the cavity from a shape close to circle to ellipse, while the volume of the cavity is kept the same. The devices are fabricated with the same principle described in *Chapter3*. The device has 200nm deep loading channel and 100nm deep cavities. We use differentially stained λ-DNA in experiment and capture the data with the Fast switching LED system which has been discussed in *Chapter4*.

7.1 Fluorescence tracking

The preprocess of the data is changed slightly for current data to minimize the dark current noise. The noise subtraction algorithm is shown pedagogically in Tang's[48] work. We use both 3 by 3 and 5 by 5 box justification and $\sigma = 3$ to

subtract the noise. The fluorescence center is tracked by Eq.5.1.1. A typical graph is shown below:

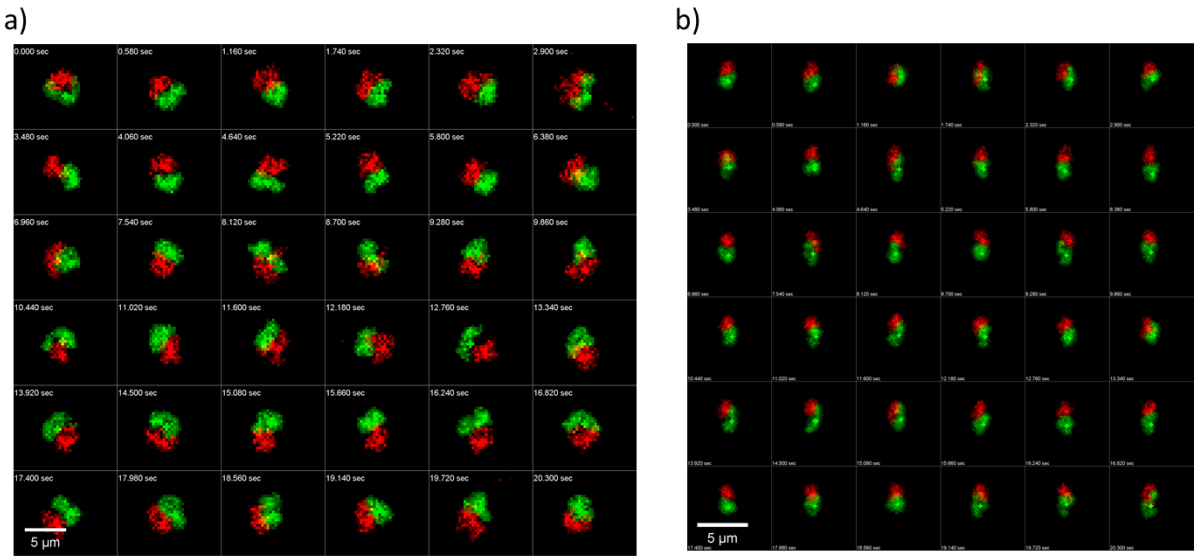

Figure 7–1: Two DNA chains trapped in an elliptical cavity with different eccentricity values. Both datasets are processed by the noise subtraction algorithm. a) The cavity eccentricity equals to 0.3. We see one swapping event within the first 10 seconds. The two chains tends to rotate around the cavity center. b) The cavity eccentricity equals to 0.9. There is no swapping event within the entire length of montage. However, two chains attempt to switch position at the 4th and 24th frame. The failure indicates that the thermal fluctuation is not high enough to overcome the free energy barrier. The small cross marked on each data frame is to validate the tracking algorithm.

We use 20ms exposure time and set the ROI such that the entire cavity in the region while the capture speed is optimized[1] . The video is sufficiently long enough that two chains system can explore nearly all the possible configurations. The noise subtraction and tracking have been implemented to ImageJ, which can improve the analysing efficiency. Position distribution for both YOYO-1 and YOYO-3 stained chain is shown below:

[1] Refer Fig.4–6 for further information

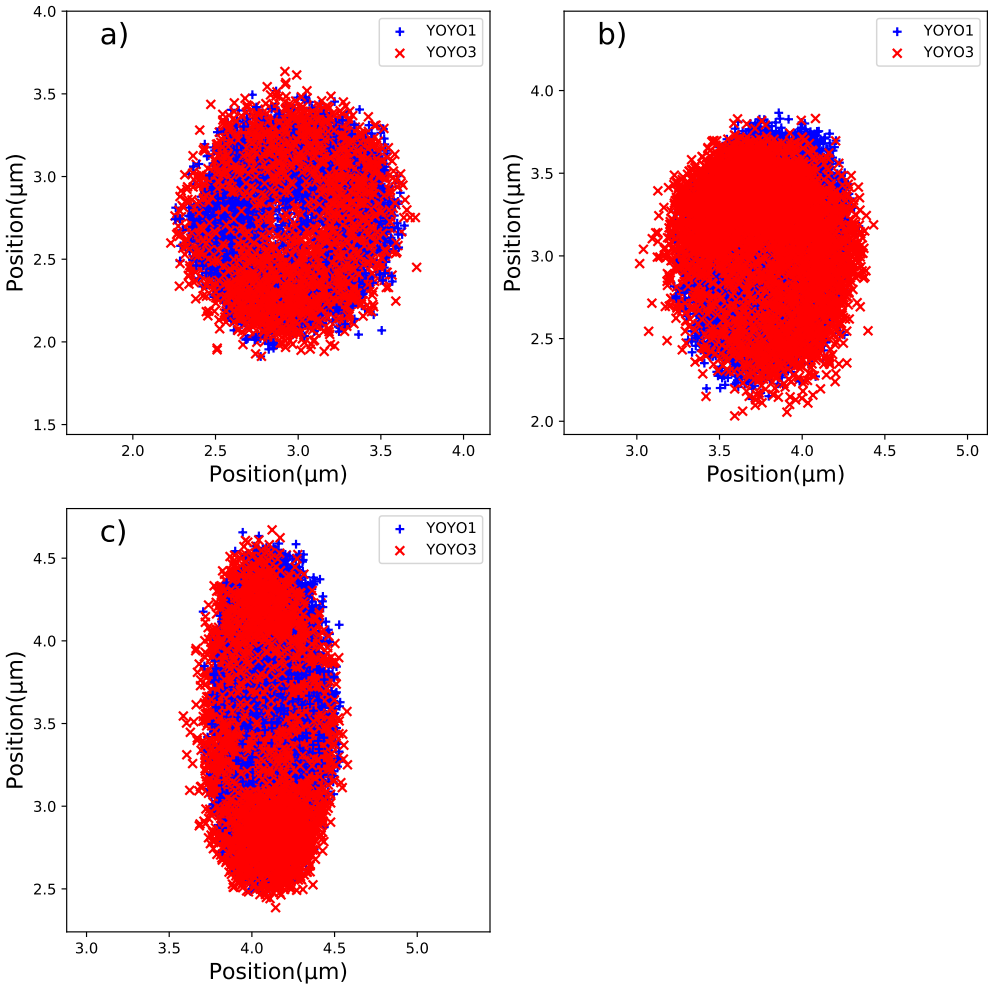

Figure 7–2: Position distribution of DNA chains labeled by YOYO-1 and YOYO-3. The data points represent the position of chain in different frames. Different cavity geometry can be observed in the graph. a) Ellipse eccentricity is 0.3. b) Ellipse eccentricity is 0.6. c) Ellipse eccentricity is 0.9. The length of our data is long enough to cover most of the possible configuration.

We observe that the two chains distribute more evenly with smaller eccentricity. In fact, as we see in Fig.7–1(b), two chains favor the polar side of the ellipse generally. They tend to appear at the cavity center only when they try to switch the position.

To transform position data to a coordinate free system, we define separation vector pointing from YOYO-3 stained chain to YOYO-1 stained chain. A plot of the distribution of this separation vector is shown in Fig.7–3. With the changing of eccentricity, the distribution shifts gradually from a more uniform distribution to uneven distribution. Due to the exclusion effect, the separation vector distribution has a "donut shape" with a hollow center. More interestingly, the separation distribution breaks the uniform symmetry between 0.6 to 0.9 eccentricity. We indicate "donut" effect with pixel scale anti-correlation in the previous study in Fig.5–6, but the time-resolution of mechanical turret is not sufficient to resolve the donut shape.

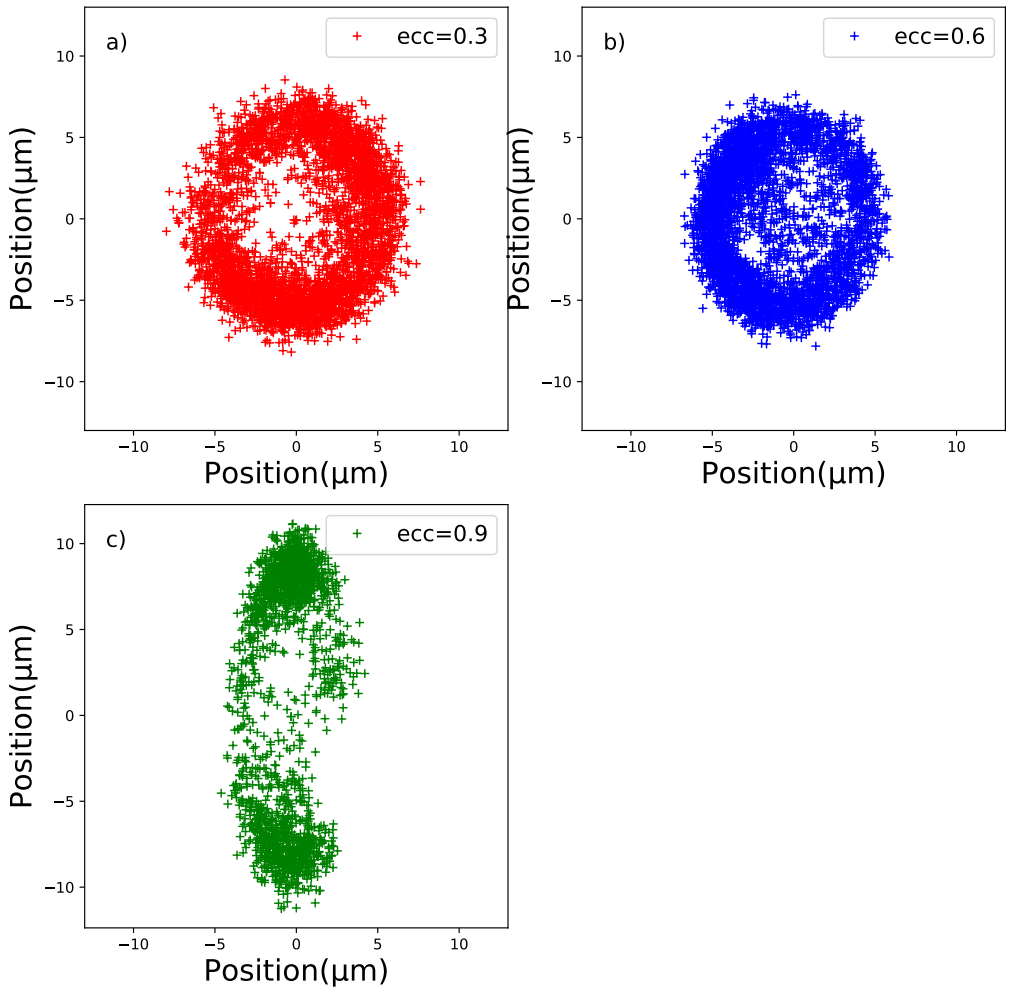

Figure 7–3: Separation vector distribution of two chains system. a) separation vector with 0.3 eccentricity. b) separation vector with 0.6 eccentricity. c) separation vector with 0.9 eccentricity. As the eccentricity becoming larger, the separation vector distribution prefers the polar region than the ellipse short axis plane.

7.2 Position correlation

The position correlation can be calculated by Eq.5.2.3 and Eq.5.2.4. Both the auto-correlation and cross-correlation can be resolved with a lot more data points.

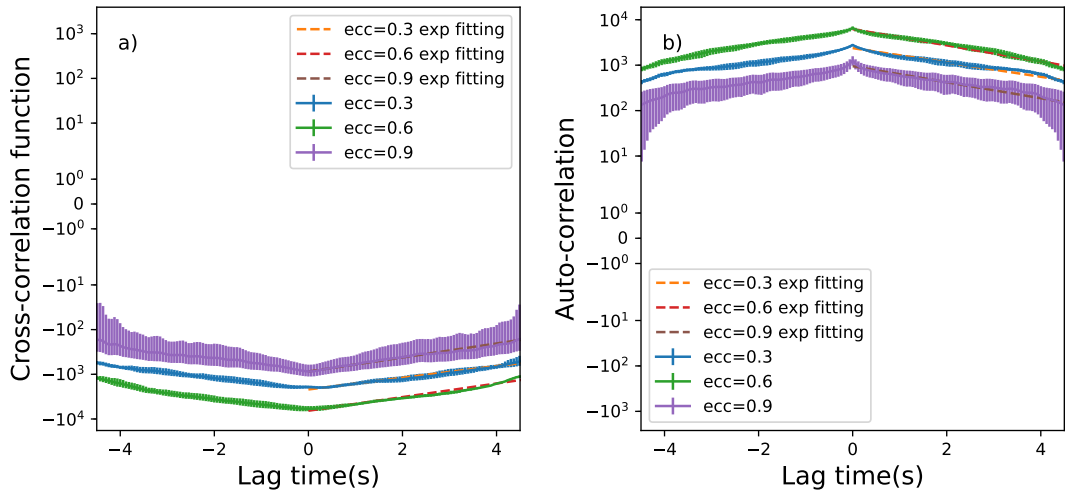

Figure 7–4: Position cross correlation and position auto correlation. Error bar is measured by taking statistics analysis over four individual video stacks. a)X-position cross-correlation of YOYO-1 and YOYO-3 stained chain. b) X-position auto-correlation of YOYO-1 stained chain. YOYO-3 stained chain behaves similarly. To reduce the redundancy, only YOYO-1 data is shown here. The data has been fitted by single exponential function to extract the decorrelation time. The fitting is plotted with dashline.

Negative cross-correlation indicates the spacial exclusive effect between the chains. The decorrelation time can be defined with the same method as in *Chapter5*. Interestingly, the decorrelation time of position cross-correlation is nearly the same with that of the auto-correlation. We hypothesize that the conformation of two chains are tightly correlated. Thus, the time it takes for two chains system to loose their joint conformation should be the same with the auto-correlation decorrelation time.

7.3 Position switching of two chains

Thermal fluctuation creates the stochastic driving force on the two chains system. The thermal contact between reservoir, which is our lab environment, and the cavity enables the fluctuation of total energy of the two chains system. The free energy landscape of two chains system can be illustrated as follow:

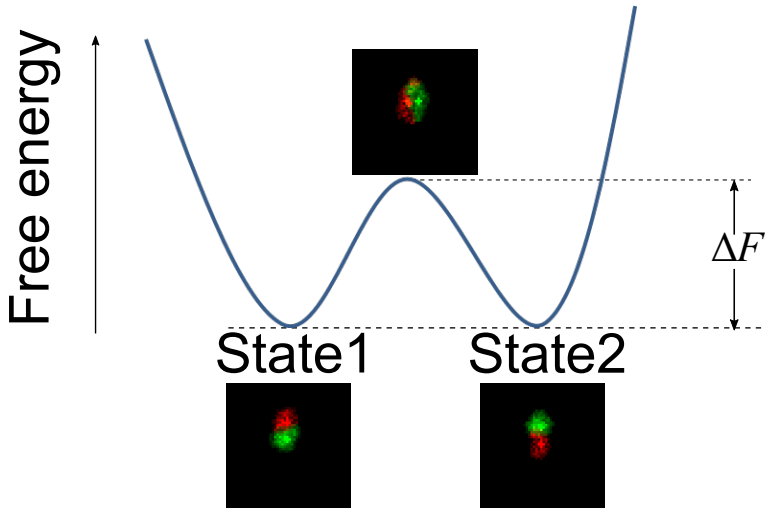

Figure 7–5: Schematic of free energy landscape of two chains system. System needs to overcome the free energy barrier when transit from state 1 to state 2.

Theoretically, state 1 and state 2 share the same free energy because of the symmetry of ellipse, which means they are two microstates with the same energy. However, system needs to overcome the free energy barrier, which has higher free energy because of the interaction between two chains, to switch from state 1 to state 2. We use the separation vector definition to characterize the switching event:

$$\overrightarrow{r}_{sep} = \overrightarrow{r}_{yoyo1} - \overrightarrow{r}_{yoyo3} \tag{7.3.1}$$

The states can be measured by the y-coordinates. The y-axis plotting is shown below:

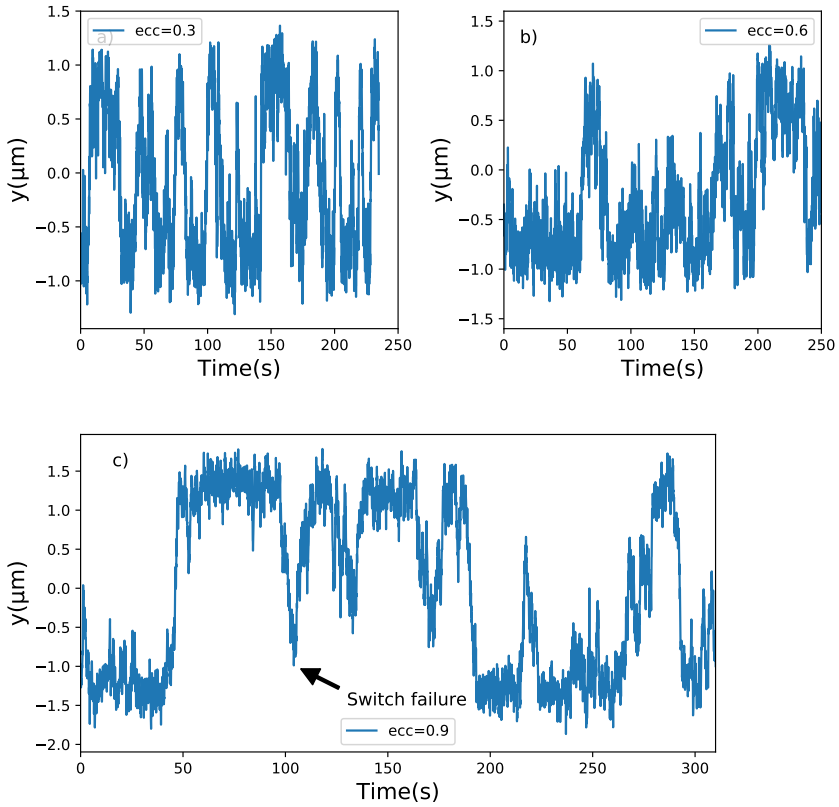

Figure 7–6: Y-coordinate of the separation vector. The base line for positive and negative value indicate the time separation vector pointing up and down respectively. a) Y-coordinate separation of data captured with 0.3 eccentricity ellipse. b) Y-axis separation of data captured with 0.6 eccentricity ellipse. c) Y-axis separation of data captured with 0.9 eccentricity ellipse.

The position switch events happens more frequently with smaller eccentricity. The short axis of the ellipse creates a tighter confinement spacing. The two chains have to extend and share the short axis spacing to switch position. The configuration of two states and switching moment are shown in Fig.7–6.

This states transition problem can be modeled by Reaction-rate theory which was firstly proposed back in 1940 by Henrik Kramer[19]. The system has been thermally activated such that the system is able to cross the barrier. However, the theory has not been adapted on multiple chains interaction system. How to couple the effect of polymer internal degree of freedom and cavity aspect ratio to free energy will be the main question. In current stage of experiment, we are still working on capture data with high eccentricity cavity, to probe the phase transition from 0D cavity to 1D nanochannel.

REFERENCES

[1] Anthony Balducci, Pan Mao, Jongyoon Han, and Patrick S Doyle. Double-stranded dna diffusion in slitlike nanochannels. *Macromolecules*, 39(18):6273–6281, 2006.

[2] Anthony Balducci, Pan Mao, Jongyoon Han, and Patrick S. Doyle. Double-stranded DNA diffusion in slitlike nanochannels. *Macromolecules*, 39(18):6273–6281, sep 2006.

[3] Jean-Christophe Baret, Oliver J Miller, Valerie Taly, Michaël Ryckelynck, Abdeslam El-Harrak, Lucas Frenz, Christian Rick, Michael L Samuels, J Brian Hutchison, Jeremy J Agresti, et al. Fluorescence-activated droplet sorting (fads): efficient microfluidic cell sorting based on enzymatic activity. *Lab on a Chip*, 9(13):1850–1858, 2009.

[4] Douwe Jan Bonthuis, Christine Meyer, Derek Stein, and Cees Dekker. Conformation and dynamics of dna confined in slitlike nanofluidic channels. *Physical review letters*, 101(10):108303, 2008.

[5] Douwe Jan Bonthuis, Christine Meyer, Derek Stein, and Cees Dekker. Conformation and dynamics of DNA confined in slitlike nanofluidic channels. *Physical Review Letters*, 101(10):108303, sep 2008.

[6] Jens B Bosse, Nikhila S Tanneti, Ian B Hogue, and Lynn W Enquist. Open led illuminator: A simple and inexpensive led illuminator for fast multicolor particle tracking in neurons. *PloS one*, 10(11):e0143547, 2015.

[7] F Brochard and Pierre-Gilles de Gennes. Dynamics of confined polymer chains. *The Journal of Chemical Physics*, 67(1):52–56, 1977.

[8] Xavier Capaldi, Zezhou Liu, Yuning Zhang, Lili Zeng, Rodrigo Reyes-Lamothe, and Walter Reisner. Probing the organization and dynamics of two dna chains trapped in a nanofluidic cavity. *Soft matter*, 2018.

[9] Y-L Chen, MD Graham, JJ de Pablo, GC Randall, M Gupta, and PS Doyle. Conformation and dynamics of single dna molecules in parallel-plate slit microchannels. *Physical Review E*, 70(6):060901, 2004.

[10] Yuhao Chen, Wancheng Yu, Jiajun Wang, and Kaifu Luo. Polymer segregation under confinement: Influences of macromolecular crowding and the interaction between the polymer and crowders. *The Journal of Chemical Physics*, 143(13):134904, oct 2015.

[11] Peter Cifra. Weak-to-strong confinement transition of semi-flexible macromolecules in slit and in channel. *The Journal of chemical physics*, 136(2):024902, 2012.

[12] Liang Dai, Jeremy J Jones, Johan RC van der Maarel, and Patrick S Doyle. A systematic study of dna conformation in slitlike confinement. *Soft Matter*, 8(10):2972–2982, 2012.

[13] M Daoud and PG De Gennes. Statistics of macromolecular solutions trapped in small pores. *Journal de Physique*, 38(1):85–93, 1977.

[14] Andrew J Demello. Microfluidics: Dna amplification moves on. *Nature*, 422(6927):28, 2003.

[15] Masao Doi. *Introduction to polymer physics*. Oxford university press, 1996.

[16] Masao Doi. *Soft Matter Physics*. Oxford University Press, jun 2013.

[17] Emmanuel Giudice, Péter Várnai, and Richard Lavery. Base pair opening within b-dna: free energy pathways for gc and at pairs from umbrella sampling simulations. *Nucleic acids research*, 31(5):1434–1443, 2003.

[18] IAIN M Hagan and JEREMY S Hyams. The use of cell division cycle mutants to investigate the control of microtubule distribution in the fission yeast schizosaccharomyces pombe. *Journal of Cell Science*, 89(3):343–357, 1988.

[19] Peter Hänggi, Peter Talkner, and Michal Borkovec. Reaction-rate theory: fifty years after kramers. *Reviews of modern physics*, 62(2):251, 1990.

[20] N. Patrick Higgins and Alexander V. Vologodskii. Topological behavior of plasmid DNA. In *Plasmids: Biology and Impact in Biotechnology and Discovery*, pages 105–131. American Society of Microbiology, 2015.

[21] David S Horowitz and James C Wang. Torsional rigidity of dna and length dependence of the free energy of dna supercoiling. *Journal of molecular biology*, 173(1):75–91, 1984.

[22] Chih-Chen Hsieh, Anthony Balducci, and Patrick S Doyle. An experimental study of dna rotational relaxation time in nanoslits. *Macromolecules*, 40(14):5196–5205, 2007.

[23] Paul J Hung, Philip J Lee, Poorya Sabounchi, Robert Lin, and Luke P Lee. Continuous perfusion microfluidic cell culture array for high-throughput cell-based assays. *Biotechnology and bioengineering*, 89(1):1–8, 2005.

[24] Andrea Idili, Francesco Ricci, and Alexis Vallée-Bélisle. Determining the folding and binding free energy of dna-based nanodevices and nanoswitches using urea titration curves. *Nucleic acids research*, 45(13):7571–7580, 2017.

[25] J Jaklevic, JA Kirby, MP Klein, AS Robertson, GS Brown, and P Eisenberger. Fluorescence detection of exafs: Sensitivity enhancement for dilute species and thin films. *Solid State Communications*, 23(9):679–682, 1977.

[26] Alec J Jeffreys, Victoria Wilson, and Swee Lay Thein. Individual-specific fingerprints of human dna. *Nature*, 316(6023):76–79, 1985.

[27] Suckjoon Jun and Andrew Wright. Entropy as the driver of chromosome segregation. *Nature Materials*, 8:600C607, 2010.

[28] Juin Kim, Chanil Jeon, Hawoong Jeong, Youngkyun Jung, and Bae-Yeun Ha. A polymer in a crowded and confined space: effects of crowder size and polydispersity. *Soft Matter*, 11(10):1877–1888, 2015.

[29] Binu Kundukad, Jie Yan, and Patrick S. Doyle. Effect of YOYO-1 on the mechanical properties of DNA. *Soft Matter*, 10(48):9721–9728, 2014.

[30] A. Kusumi, Y. Sako, and M. Yamamoto. Confined lateral diffusion of membrane receptors as studied by single particle tracking (nanovid microscopy). effects of calcium-induced differentiation in cultured epithelial cells. *Biophysical Journal*, 65(5):2021–2040, nov 1993.

[31] Thomas MH Lee, Debbie HY Lee, Connie YN Liaw, Alex IK Lao, and I-Ming Hsing. Detailed characterization of anodic bonding process between glass and thin-film coated silicon substrates. *Sensors and Actuators A: Physical*, 86(1-2):103–107, 2000.

[32] Po-Keng Lin, Chi-Cheng Fu, Y.-L. Chen, Yan-Ru Chen, Pei-Kuen Wei, C. H. Kuan, and W. S. Fann. Static conformation and dynamics of single DNA molecules confined in nanoslits. *Physical Review E*, 76(1):011806, jul 2007.

[33] Po-Keng Lin, Keng-hui Lin, Chi-Cheng Fu, K-C Lee, Pei-Kuen Wei, Woei-Wu Pai, Pei-Hsi Tsao, Y-L Chen, and WS Fann. One-dimensional dynamics and transport of dna molecules in a quasi-two-dimensional nanoslit. *Macromolecules*, 42(5):1770–1774, 2009.

[34] Y. L. Lyubchenko and L. S. Shlyakhtenko. Visualization of supercoiled DNA with atomic force microscopy in situ. *Proceedings of the National Academy of Sciences*, 94(2):496–501, jan 1997.

[35] Andres W Martinez, Scott T Phillips, George M Whitesides, and Emanuel Carrilho. Diagnostics for the developing world: microfluidic paper-based analytical devices, 2009.

[36] Matthias Mehling and Savaş Tay. Microfluidic cell culture. *Current opinion in Biotechnology*, 25:95–102, 2014.

[37] Theo Odijk. The statistics and dynamics of confined or entangled stiff polymers. *Macromolecules*, 16(8):1340–1344, 1983.

[38] Theo Odijk. Scaling theory of dna confined in nanochannels and nanoslits. *Physical Review E*, 77(6):060901, 2008.

[39] James Pelletier, Ken Halvorsen, Bae-Yeun Ha, Raffaella Paparcone, Steven J. Sandler, Conrad L. Woldringh, Wesley P. Wong, and Suckjoon Jun. Physical manipulation of the escherichia coli chromosome reveals its soft nature. *Proceedings of the National Academy of Sciences*, 109(40):E2649–E2656, 2012.

[40] Walter Reisner, Jason P Beech, Niels B Larsen, Henrik Flyvbjerg, Anders Kristensen, and Jonas O Tegenfeldt. Nanoconfinement-enhanced conformational response of single dna molecules to changes in ionic environment. *Physical review letters*, 99(5):058302, 2007.

[41] Walter Reisner, Keith J Morton, Robert Riehn, Yan Mei Wang, Zhaoning Yu, Michael Rosen, James C Sturm, Stephen Y Chou, Erwin Frey, and Robert H Austin. Statics and dynamics of single dna molecules confined in nanochannels. *Physical Review Letters*, 94(19):196101, 2005.

[42] Takahiro Sakaue. Semiflexible polymer confined in closed spaces. *Macromolecules*, 40(14):5206–5211, jul 2007.

[43] Ji Wook Shim, Qiulin Tan, and Li-Qun Gu. Single-molecule detection of folding and unfolding of the g-quadruplex aptamer in a nanopore nanocavity. *Nucleic acids research*, 37(3):972–982, 2008.

[44] Douglas E. Smith, Thomas T. Perkins, and Steven Chu. Dynamical scaling of DNA diffusion coefficients. *Macromolecules*, 29(4):1372–1373, jan 1996.

[45] Derek Stein, Frank HJ van der Heyden, Wiepke JA Koopmans, and Cees Dekker. Pressure-driven transport of confined dna polymers in fluidic channels. *Proceedings of the National Academy of Sciences*, 103(43):15853–15858, 2006.

[46] Elizabeth A Strychalski, Stephen L Levy, and Harold G Craighead. Diffusion of dna in nanoslits. *Macromolecules*, 41(20):7716–7721, 2008.

[47] Elizabeth A. Strychalski, Stephen L. Levy, and Harold G. Craighead. Diffusion of DNA in nanoslits. *Macromolecules*, 41(20):7716–7721, oct 2008.

[48] Jing Tang, Stephen L Levy, Daniel W Trahan, Jeremy J Jones, Harold G Craighead, and Patrick S Doyle. Revisiting the conformation and dynamics of dna in slitlike confinement. *Macromolecules*, 43(17):7368–7377, 2010.

[49] Lasse H Thamdrup, Anna Klukowska, and Anders Kristensen. Stretching dna in polymer nanochannels fabricated by thermal imprint in pmma. *Nanotechnology*, 19(12):125301, 2008.

[50] Douglas R Tree, Wesley F Reinhart, and Kevin D Dorfman. The odijk regime in slits. *Macromolecules*, 47(11):3672–3684, 2014.

[51] Hitoshi Uemura, Masatoshi Ichikawa, and Yasuyuki Kimura. Crossover behavior in static and dynamic properties of a single dna molecule from three to quasi-two dimensions. *Physical Review E*, 81(5):051801, 2010.

[52] Frank Uhlmann. Smc complexes: from dna to chromosomes. *Nature Reviews Molecular Cell Biology*, 17(7):399–412, 2016.

[53] Pawel Utko, Fredrik Persson, Anders Kristensen, and Niels B Larsen. Injection molded nanofluidic chips: fabrication method and functional tests using single-molecule dna experiments. *Lab on a Chip*, 11(2):303–308, 2011.

[54] G. Voordouw, Z. Kam, N. Borochov, and H. Eisenberg. Isolation and physical studies of the intact supercoiled. *Biophysical Chemistry*, 8(2):171–189, may 1978.

[55] Kirt R Williams and Richard S Muller. Etch rates for micromachining processing. *Journal of Microelectromechanical systems*, 5(4):256–269, 1996.

[56] Hiromi Yamakawa and Motoharu Fujii. Wormlike chains near the rod limit: Path integral in the wkb approximation. *The Journal of Chemical Physics*, 59(12):6641–6644, 1973.

[57] C Zhang, G Hatipoglu, and S Tadigadapa. A modified inductively coupled plasma for high-speed, ultra-smooth reactive phase etching of silica glass. In *Solid-State Sensors, Actuators and Microsystems (TRANSDUCERS), 2015 Transducers-2015 18th International Conference on*, pages 592–595. IEEE, 2015.